

Close, bright and boxy: the superluminous SN 2018hti

A. Fiore,^{1*} S. Benetti,¹ M. Nicholl,^{2,3} A. Reguitti,^{4,5,1} E. Cappellaro,¹ S. Campana,⁶ S. Bose,^{7,8} E. Paraskeva,^{9,10,11,38} E. Berger,¹² T. M. Bravo,¹³ J. Burke,^{14,15} Y.-Z. Cai,¹⁶ T.-W. Chen,¹⁷ P. Chen,¹⁸ R. Ciolfi,^{1,19} S. Dong,¹⁸ S. Gomez,²⁰ M. Gromadzki,²¹ C. P. Gutiérrez,^{22,23} D. Hiramatsu,^{14,15,39,40} G. Hosseinzadeh,²⁴ D. A. Howell,^{14,15} A. Jerkstrand,¹⁷ E. Kankare,²⁵ A. Kozyreva,²⁶ K. Maguire,²⁷ C. McCully,¹⁴ P. Ochner,^{1,28} C. Pellegrino,^{14,15} G. Pignata,^{4,5} R. S. Post,²⁹ N. Elias-Rosa,^{1,30} M. Shahbandeh,³¹ S. Schuldt,^{26,32} B. P. Thomas,³³ L. Tomasella,¹ J. Vinkó,^{33,34,35,36} C. Vogl,²⁶ J. C. Wheeler,³³ D. R. Young³⁷

¹INAF – Osservatorio Astronomico di Padova, Vicolo dell’Osservatorio 5, I-35122 Padova, Italy

²Birmingham Institute for Gravitational Wave Astronomy and School of Physics and Astronomy, University of Birmingham, Birmingham B15 2TT, UK

³Institute for Astronomy, University of Edinburgh, Royal Observatory, Blackford Hill, EH9 3HJ, UK

⁴Departamento de Ciencias Físicas – Universidad Andres Bello, Avda. República 252, Santiago, Chile

⁵Millennium Institute of Astrophysics, Nuncio Monseñor Sótero Sanz 100, Providencia, Santiago, Chile

⁶INAF – Osservatorio Astronomico di Brera, Via Bianchi 46, I-23807 Merate, Italy

⁷Department of Astronomy, The Ohio State University, 140 W. 18th Avenue, Columbus, OH 43210, USA

⁸Center for Cosmology and AstroParticle Physics (CCAPP), The Ohio State University, 191 W.Woodruff Avenue, Columbus, OH 43210, USA

⁹IAASARS, National Observatory of Athens, 15236, Penteli, Greece

¹⁰Department of Astrophysics, Astronomy & Mechanics, Faculty of Physics, National and Kapodistrian University of Athens, 15784 Athens, Greece

¹¹Nordic Optical Telescope, Apartado 474, E-38700 Santa Cruz de La Palma, Santa Cruz de Tenerife, Spain

¹²Center for Astrophysics | Harvard & Smithsonian, 60 Garden Street, Cambridge, MA 02138-1516, USA

¹³School of Physics and Astronomy, University of Southampton, Southampton, Hampshire, SO17 1BJ, UK

¹⁴Las Cumbres Observatory, 6740 Cortona Dr. Suite 102, Goleta, CA, 93117, USA

¹⁵Department of Physics, University of California, Santa Barbara, Santa Barbara, CA, 93106, USA

¹⁶Physics Department and Tsinghua Center for Astrophysics (THCA), Tsinghua University, Beijing, 100084, China

¹⁷The Oskar Klein Centre, Department of Astronomy, Stockholm University, AlbaNova, SE-10691 Stockholm, Sweden

¹⁸Kavli Institute for Astronomy and Astrophysics, Peking University, Yi He Huan Road 5, Hai Dian District, Beijing 100871, China

¹⁹INFN – Sezione di Padova, Via Francesco Marzolo 8, I-35131 Padova, Italy

²⁰Space Telescope Science Institute, 3700 San Martin Drive, Baltimore, MD 21218, USA

²¹Astronomical Observatory, University of Warsaw, Al. Ujazdowskie 4, 00-478 Warszawa, Poland

²²Finnish Centre for Astronomy with ESO (FINCA), FI-20014 University of Turku, Finland

²³Tuorla Observatory, Department of Physics and Astronomy, FI-20014 University of Turku, Finland

²⁴Steward Observatory, University of Arizona, 933 North Cherry Avenue, Tucson, AZ 85721-0065, USA

²⁵Department of Physics and Astronomy, University of Turku, FI-20014 Turku, Finland

²⁶Max-Planck-Institut für Astrophysik, Karl-Schwarzschild-Str. 1, D-85748, Garching, Germany

²⁷School of Physics, Trinity College Dublin, The University of Dublin, Dublin 2, Ireland

²⁸Dipartimento di Fisica e Astronomia G. Galilei , Università di Padova, Vicolo dell’Osservatorio 3, I-35122 Padova, Italy

²⁹Post Astronomy, Lexington, MA, USA

³⁰Institute of Space Sciences (ICE, CSIC), Campus UAB, Carrer de Can Magrans s/n, 08193 Barcelona, Spain

³¹Department of Physics, Florida State University, 77 Chieftan Way, Tallahassee, FL 32306, USA

³²Technische Universität München, Physik Department, James-Franck Str. 1, 85748 Garching, Germany

³³Department of Astronomy, University of Texas at Austin, 2515 Speedway, Stop C1400, Austin, Texas 78712-1205, USA

³⁴Konkoly Observatory, CSFK, Konkoly-Thege M. út 15-17, Budapest, 1121, Hungary

³⁵ELTE Eötvös Loránd University, Institute of Physics, Pázmány Péter sétány 1/A, Budapest, 1117 Hungary

³⁶Department of Optics & Quantum Electronics, University of Szeged, Dóm tér 9, Szeged, 6720, Hungary

³⁷Astrophysics Research Centre, School of Mathematics and Physics, Queen’s University Belfast, Belfast BT7 1NN, UK

³⁸Department of Physics and Astronomy, Aarhus University, Ny Munkegade 120, DK-8000 Aarhus C, Denmark

³⁹Center for Astrophysics | Harvard & Smithsonian, 60 Garden Street, Cambridge, MA 02138-1516, USA

⁴⁰The NSF AI Institute for Artificial Intelligence and Fundamental Interactions

ABSTRACT

SN 2018hti was a very nearby ($z = 0.0614$) superluminous supernova with an exceedingly bright absolute magnitude of -21.7 mag in r -band at maximum. The densely sampled pre-maximum light curves of SN 2018hti show a slow luminosity evolution and constrain the rise time to ~ 50 rest-frame days. We fitted synthetic light curves to the photometry to infer the physical parameters of the explosion of SN 2018hti for both the magnetar and the CSM-interaction scenarios. We conclude that one of two mechanisms could be powering the luminosity of SN 2018hti; interaction with $\sim 10 M_{\odot}$ of circumstellar material or a magnetar with a magnetic field of $B_p \sim 1.3 \times 10^{13}$ G and initial period of $P_{\text{spin}} \sim 1.8$ ms. From the nebular spectrum modelling we infer that SN 2018hti likely results from the explosion of a $\sim 40 M_{\odot}$ progenitor star.

Key words: Transients:supernovae — supernova:general — supernovae:individual:SN 2018hti.

1 INTRODUCTION

It is widely accepted that the explosion of massive stars ($\gtrsim 8 M_{\odot}$, e. g. Smartt 2009) is triggered by the gravitational collapse of their cores. This leads to a core-collapse supernova (SN) explosion, whose light curves (LCs) reach an absolute magnitude at maximum usually ranging between -14 and -19 mag (e.g. Richardson et al. 2014; Modjaz et al. 2019) in optical bands. These luminosities are suitably explained with the decay of $< 0.1 M_{\odot}$ of ^{56}Ni (e. g. Nadyozhin 1994; Müller et al. 2017; Anderson 2019; Prentice et al. 2019) and with the thermal energy deposited in the progenitor’s envelope during the gravitational collapse. The discoveries of superluminous supernovae (SLSNe) with an absolute magnitude even brighter than -21 mag (e.g. Gal-Yam 2012; Howell 2017; Gal-Yam 2019a) challenge this standard supernova paradigm. In fact, $\gtrsim 5 M_{\odot}$ of ^{56}Ni would be required to account for these luminosities (e.g. Kasen et al. 2011; Dessart et al. 2012).

Apart from their exceptional brightness, SLSNe are characterised by their pre-maximum/maximum optical spectra, usually showing a hot ($\gtrsim 15000$ K) continuum. Similar to the classical SNe (Minkowski 1941), SLSNe are sub-classified as SLSNe I and SLSNe II depending on whether they are hydrogen deficient or hydrogen rich, respectively (Gal-Yam 2012). In addition, SLSNe IIn are characterized by the presence of multicomponent/narrow Balmer emission lines in their spectra and most likely fill the high luminosity tail of the luminosity function of SNe IIn (Gal-Yam 2012).

SLSNe I are usually discovered in metal-poor and star-forming host galaxies (Chen et al. 2013; Lunnan et al. 2014; Leloudas et al. 2015; Perley et al. 2015; Chen et al. 2017a; Schulze et al. 2018). They are recognized by the presence of prominent absorptions between 3000–5000 Å in their pre-maximum/maximum optical spectra. This is an almost unique feature of SLSNe I, usually identified as the contribution of O II transitions (e. g. Quimby et al. 2011; Mazzali et al. 2016; Gal-Yam 2019b), although this identification has been questioned (e.g. Könyves-Tóth & Vinkó 2020). However, these features were observed also in the SN Ib SN 2008D (Soderberg et al. 2008), and in the recently-proposed SN subclass of SNe Icn (Gal-Yam et al. 2021; Pastorello et al. 2021) and in the type-II SN 2019hcc (Parrag et al. 2021). 15–20 days after maximum luminosity, the spectra of SLSNe I start to remarkably reproduce the behaviour of SNe Ic and SNe Ic broad lined (SNe Ic BL) at maximum luminosity (e.g. Pastorello et al. 2010). Interestingly, recent discoveries of SLSNe I and SNe Ic appear to fill the luminosity gap between these two subclasses (such as the cases of the luminous SNe Ic SN 2012aa, SN 2019stc, Roy et al. 2016, Gomez et al. 2021). The physical explanation linking these SN

subclasses is still a matter of investigations (e. g. Zou & Cheng 2018; Blanchard et al. 2019; Lin et al. 2020b). The photometric evolution of SLSNe I is more heterogeneous: LCs of SLSNe I typically evolve either smoothly (e. g. SN 2010gx, SN 2011ke, Pastorello et al. 2010; Inserra et al. 2013) or they can show a complex behaviour with pre-/post-maximum bumps (e.g. SN 2015bn, iPTF15esb, SN 2017gci, SN 2018don, Nicholl et al. 2015b; Yan et al. 2015; Angus et al. 2019; Lunnan et al. 2020; Fiore et al. 2021, see also Hosseinzadeh et al. 2021). Their LCs evolve over a very broad range of timescales; a diversity which prompted the community to propose a slow/fast-evolving sub-classification of SLSNe I events, but the discovery of intermediate objects (e. g. Gaia16apd, SN 2017gci, Kangas et al. 2017; Yan et al. 2017a; Nicholl et al. 2017a; Fiore et al. 2021; Stevance & Eldridge 2021) and statistical studies (Nicholl et al. 2015a; De Cia et al. 2018; Lunnan et al. 2018b; Angus et al. 2019) point towards a continuous distribution between the two sub-categories.

There is no general consensus about the engine powering SLSNe (see Moriya et al. 2018, for a recent review). Several scenarios have been proposed to explain the huge luminosities of SLSNe I: (i) the magnetar scenario, which considers the contribution of the radiation-dominated wind inflated by a spinning down millisecond magnetar (e.g. Kasen & Bildsten 2010; Woosley 2010; Inserra et al. 2013; Wang et al. 2015; Chen et al. 2015, 2017b, 2016; Nicholl et al. 2017b; Margalit et al. 2018; Vurm & Metzger 2021); (ii) the interaction of the SN ejecta with shells of circumstellar material (CSM, e.g. Chevalier & Fransson 2003; Chevalier & Irwin 2011; Ginzburg & Balberg 2012; Chatzopoulos et al. 2013; Nicholl et al. 2014; Smith 2017; Lunnan et al. 2018a, 2020; Nicholl et al. 2020) lost by the progenitor star prior to its explosion via stellar winds or alternatively via the pulsational-pair instability phenomenon (e.g. Woosley et al. 2007; Woosley 2017; Renzo et al. 2020); (iii) the pair-instability scenario, where e^+ , e^- pair creation in a very massive star (with a He-core mass $64 M_{\odot} \lesssim M_{\text{He}} \lesssim 133 M_{\odot}$, e.g. Heger & Woosley 2002) induces the collapse of the star and triggers a thermonuclear runaway in the core, allowing for a massive production of ^{56}Ni . CSM interaction is usually invoked as the major power source for (SL)SNe IIn (as in the case of SN 2006gy, Smith & McCray 2007; Smith et al. 2007; Agnoletto et al. 2009) as it provides a suitable explanation for the narrow/multicomponent features usually seen in their spectra. SLSNe I LCs can be reasonably well explained by CSM models too (e. g. Chevalier & Fransson 2003; Chevalier & Irwin 2011; Ginzburg & Balberg 2012; Chatzopoulos et al. 2013), although the SLSNe I spectra lack for strong interaction signatures. However, it has been shown (Chevalier & Irwin 2011; Moriya & Tominaga 2012; Smith et al. 2015; Andrews & Smith 2018; Bhirombhakdi et al. 2019) that a buried CSM interaction might suppress these features under specific conditions, e. g. if the SN progenitor star is surrounded by a CSM

* E-mail: achillefiore@gmail.com

disk (Smith 2017). The complexities in some SLSNe LCs are also indicative of CSM interaction. While the simplest explanation for these complexities is late-time interaction with shells or clumps of CSM (e.g. Moriya et al. 2018), Metzger et al. (2014) argue that they can be mimicked by the opacity variations due to wind-driven ionisation fronts of a millisecond magnetar.

In this work, we present and discuss the spectrophotometric observations of SLSN I SN 2018hti, located at RA = $03^{\text{h}} 40^{\text{m}} 53.76^{\text{s}}$, Dec = $+11^{\circ} 46' 37.17''$. SN 2018hti was discovered on 2018 November 1 by the Asteroid Terrestrial-impact Last Alert System (ATLAS) project (Tonry et al. 2018a,b) and initially named ATLAS18yff. It was then classified on 2018 November 6 by Burke et al. (2018) as a SLSN I. Independent spectro-photometric data of SN 2018hti are already presented by Lin et al. (2020a) and imaging polarimetry data of SN 2018hti are presented by Lee (2019). Here we present the photometric and spectroscopic data of SN 2018hti in Sec. 2 and Sec. 3, respectively. We discuss in Sec. 4 the spectro-photometric data of SN 2018hti: in particular, the metallicity measurements of its host galaxy (Sec. 4.1), the blackbody temperature and radius evolutions (Sec. 4.2), the photospheric velocity (Sec. 4.3), some photometric and spectroscopic comparisons of SN 2018hti with a selected sample of SLSNe I (Sec. 4.4) and finally the suitability of magnetar and of CSM-interaction scenarios for SN 2018hti (Sec. 4.5).

In the following, we will assume a flat Universe with $H_0 = 71 \pm 3 \text{ km s}^{-1} \text{ Mpc}^{-1}$, $\Omega_\Lambda = 0.69$, $\Omega_M = 0.31$ (taking an average of H_0 among the estimates provided by Planck Collaboration et al. 2016; Khetan et al. 2021; Riess et al. 2021). Hence, the redshift $z = 0.0614$ (see Sect. 3) measured with the narrow emission lines from the host galaxy corresponds to a luminosity distance $d_L = 271.2_{-11}^{+12} \text{ Mpc}$.

2 PHOTOMETRY

2.1 Observations and data reduction

We led the multi-band photometric follow up of SN 2018hti via several facilities. Ultraviolet ($uvw2, uvm2, uvw1$) and U, B, V imaging was obtained with the *Neil Gehrels Swift Observatory*+UVOT (Gehrels et al. 2004). Optical/near-infrared (NIR) $u, B, g, V, r, i, z, J, H, K_s$ photometric follow-up was obtained via the NOT Unbiased Transient Survey¹ (NUTS/NUTS2, Mattila et al. 2016; Holmbo et al. 2019) at the 2.56-m Nordic Optical Telescope (NOT)+ALFOSC/NOTCam at the Roque de los Muchachos Observatory, La Palma (Spain), the 1.82m Copernico Telescope+AFOSC and Schmidt Telescopes at the Asiago Astrophysical Observatory (Italy), the 1.2 meters telescope at the Fred Lawrence Whipple Observatory+KeplerCam and the 0.6/0.8-meter telescopes at the Post Observatory (CA, USA) and Post Observatory Mayhill (NM, USA). We also include the the Asteroid Terrestrial-impact Last Alert System (ATLAS)-photometry, the early ZTF public photometry available via the IRSA² archive and Las Cumbres Observatory (LCO)-network³ U, B, g, V, r, i photometry. LCO data (Brown et al. 2013) come from the Global Supernova Project. ATLAS- o and c magnitudes were converted to standard Sloan g - and r -filter following Tonry et al. (2018a, cfr. equation 2 therein) and Tonry et al. (2012, cfr. equation 6 and Tab. 6 therein). As the colour transformations used within these equations are determined from a stellar spectral energy distribution

(SED), the conversion tends to increase the uncertainty of the resulting magnitudes. Also, at very early epochs the $g - r$ colour was estimated via a colour extrapolation since the coeval g, r -filter photometry is not available. Lastly, we included the mid-infrared (MIR) photometry observed with the Wide-field Infrared Survey Explorer (WISE) NASA mission in the $W1$ and $W2$ wavelength bands.

Photometry was performed with the ECSNOOPY package⁴ (Cappellaro 2014) using the point spread function (PSF) fitting technique. A detailed description of the image-processing procedures can be found in Fiore et al. (2021). In particular, for SN 2018hti we removed the background contamination using the template-subtraction technique in the $u, U, B, g, V, r, i, z, W1, W2$ -filter images. This was performed with ECSNOOPY via HOTPANTS (Becker 2015). Suitable deep template u, U, B, V -filter frames were obtained at the NOT via NUTS2 on 2020 February 25, namely 414 rest-frame days after maximum light and we used PanSTARRS g, r, i, z pre-explosion images as template frames. We assumed that SN 2018hti already faded well below the detection limit and used these frames as templates. The $W1, W2$ frames used as template frames for the WISE photometry were obtained by the WISE mission on 2018 August 18, 19 (MJD=58348.35, 58349.47), i. e. before the explosion of SN 2018hti. For the NIR frames, the background level was interpolated with a low-order polynomial since no suitable deep template frame in J, H, K_s band was available. B, g, V, r, i, z magnitudes were calibrated having evaluated the photometric zero points and colour terms with a sequence of field stars from the Pan-STARRS (Panoramic Survey Telescope and Rapid Response System, Chambers et al. 2016) catalogue. The WISE magnitudes were calibrated with their instrumental zero-points. Calibrated PanSTARRS magnitudes were converted to standard SDSS system following Tonry et al. (2012, see equation 6). u magnitudes could not be calibrated with the SDSS survey as SN 2018hti was located outside of its sky coverage. Hence we calibrated the u magnitudes of the local field stars against u -band photometry of Sloan standards fields take on the same photometric night. For U, B, V images the calibration was done after converting the Pan-STARRS magnitudes to Sloan magnitudes as before, and then from Sloan magnitudes to Johnson system following Chonis & Gaskell (2008). NIR magnitudes were calibrated with a local sequence of stars from the Two-Micron All Sky Survey (Skrutskie et al. 2006). *Swift*/UVOT $uvw2, uvm2, uvw1, U, B, V$ -filter magnitudes were measured by stacking the layers of the individual observing segments with the task UVOTIMSUM. We then measured the brightness using a 2 arcsec-radius aperture with the task UVOTSOURCE task in HEASOFT version 6.25 ((HEASARC) 2014). To calibrate the *Swift*/UVOT magnitudes, we used the recently-updated version (November 2020) of the sensitivity corrections. We also analysed data from the *Swift* X-ray telescope by first stacking all 29 UVOT exposures. The total amount of observing time amounts to 52.3 ks. No source was detected at the location of SN 2018hti. The 3σ upper limit on the 0.3–10 keV count rate at the SN position is 6.6×10^{-4} counts s^{-1} . Assuming a power-law X-ray spectrum and the Galactic column density of $1.6 \times 10^{21} \text{ cm}^{-2}$ and the distance given in Sec. 1, we derive an upper limit on the 0.3–10 keV unabsorbed luminosity of $4 \times 10^{41} \text{ erg s}^{-1}$. This is the maximum mean luminosity the SN could have had during the entire *Swift* campaign. Under the hypothesis that the putative X-ray emission follows the UV emission, we restricted our analysis to a time interval centred on the UV peak time in a ± 6 d around maximum. We selected 5 observations for a total exposure

¹ <http://nmts2.sn.ie>.

² <https://irsa.ipac.caltech.edu/>.

³ <https://lco.global/>.

⁴ ECSNOOPY is a package for SN photometry using PSF fitting and/or template subtraction developed by E. Cappellaro. A package description can be found at <http://sngroup.oapd.inaf.it/ecsnoopy.html>.

time of 7.9 ks. The SN is still undetected with a 3σ upper limit on the 0.3–10 keV count rate of 4.7×10^{-3} counts s $^{-1}$, corresponding to a 0.3–10 keV unabsorbed luminosity of 3×10^{42} erg s $^{-1}$.

Each instrument used for the observational follow-up has its own instrumental throughput. This difference introduces systematic errors when magnitudes are obtained with multiple instruments. To account for this effect, we compute the B, V, g, r, i S-corrections (Stritzinger et al. 2002) for each instrumental configuration using the observed optical spectra of SN 2018hti (similar to Pignata et al. 2004; Elias-Rosa et al. 2006; Fiore et al. 2021) and propagated this into the calculation of the pseudo-bolometric LC. However, we noticed that this correction does not affect our analysis. The resulting S-correction for the B, V, g, r, i filters and for each instrumental setup is shown in Fig. 1. For the u, U, z, J, H, K_s filters (which are not covered by the observed optical/NIR spectra), we repeated the above procedure for a set of blackbody spectra shifted to the observer frame of SN 2018hti. The blackbody spectra have temperatures spanning a range of 8000–25000 K which broadly agrees with the best-fit blackbody temperatures of the spectra of SN 2018hti (see Sec. 4.2). In this way, the S-corrections computed for the blackbody spectra provide an estimate of the S-correction outside the optical range. Unfortunately, this approach does not account for the presence of broad emission lines in the SN spectrum, which may alter the estimate of the S-correction. Synthetic-photometry measurements on the two available UV/NIR maximum/post-maximum spectra of other SLSNe I (Gaia16apd, Kangas et al. 2017, and a NIR spectrum of the SN Ic BL SN 1998bw) show that the S-corrections computed on the spectra agree with those computed on their blackbody fit within ~ 0.05 mag for the z, J, H, K_s filters. In the u and U bands, the blackbody approximation overcorrects the magnitudes with respect to the spectra of Gaia16apd (probably due to the line blanketing). This is true also for the NOTCam S-corrections calculated on the NIR IRTF+SpeX spectrum. To carefully account for this effect requires a denser and better-sampled spectroscopic follow-up outside the optical range, which at the moment has not been done for SLSNe. We therefore opted for the conservative approach of propagating the maximum S-correction ΔS_{corr} computed for the blackbody fits into the error of the pseudo-bolometric LC calculation (see Sec. 2.3).

The reduced $uvw2, uvm2, uvw1, u, U, B, g, V, r, i, z, J, H, K_s, W1, W2$ magnitudes are reported in Tab. A1, A2, A3, A4, A5. The S-corrections S_{corr} and the ΔS_{corr} values are listed in Tab. A6, A7, A8, A9, A10.

2.2 K-corrections

We computed the K -corrections of SN 2018hti for the B, V, g, r, i -filter magnitudes performing synthetic photometry measurements onto the observed-frame ($m_{s,\text{obs}}$) and rest-frame ($m_{s,\text{rest}}$) optical spectra (see Sec. 3). These were performed with the PYSPHOT PYTHON package⁵. For each filter and each spectrum, the K -corrections were computed as $K = m_{s,\text{obs}} - m_{s,\text{rest}}$ and are listed in Tab. A11. The measured K -corrections are linearly interpolated to the epochs of the imaging observation and subsequently subtracted from the magnitudes of SN 2018hti as measured on those images. $uvw2, uvm2, uvw1, u, U, z, J, H, K_s$ K -corrections were estimated using the SED blackbody fits in place of the observed spectra.

⁵ <https://pysynphot.readthedocs.io/>.

2.3 Observed and pseudo-bolometric light curves

The UV-optical-NIR observed LCs of SN 2018hti are shown in Fig. 2 and are plotted against the phase corrected for time dilation. To estimate the maximum luminosity epoch, we fit a fourth order polynomial to the r -band LC and infer a magnitude at maximum $r_{\text{max}} \simeq 16.5 \pm 0.2$ mag at MJD = 58 464.5 ± 4.0 (in agreement with the maximum found by Lin et al. 2020a). Given a distance modulus $\mu = 37.17 \pm 0.1$ mag and a Galactic extinction⁶ $A_V = 1.280$ mag (Schlafly & Finkbeiner 2011), assuming the extinction law $A_V = 3.1 \times E(B - V)$ (Cardelli et al. 1988, 1989), the absolute peak r -filter magnitude is $M_r = -21.7 \pm 0.2$ mag. We assume no internal extinction from the host galaxy, supported by the absence of the interstellar Na I D doublet and by the fact that the H α /H β ratio remains similar to the expected value for case-B recombination (Groves et al. 2012).

The earliest ATLAS detection was obtained on 2018 October 22 (MJD = 58 413.54) and the last ATLAS detection limit was exactly three days before (MJD = 58 410.54). If we assume that the latter is a genuine non detection, this provides an estimate of the explosion epoch of MJD = 58 412.04 ± 1.5. With this, the maximum-luminosity epoch implies a rest-frame rise time of $\tau_{\text{rise}} = 50 \pm 6$ days, which is typical of the slow-evolving SLSNe I (Inserra 2019). Finally, after ~ 100 days from maximum light, SN 2018hti disappeared behind the Sun. For each filter, the LC evolution is characterized by a relatively slow rise to maximum and a post-maximum decline rate of $\sim 1-2 \times \tau_{\text{rise}}$ in each filter. Moreover, the r -filter LC apparently shows a levelled off start at earliest phases, which is hard to reconcile with the overall trend of the LC. However, as noticeable in Fig. 2, the very early detections in r -filter were retrieved by the o -filter ATLAS magnitudes whose colour transformations is uncertain. For this reason we also show the observed ATLAS o -filter LC in Fig. 3 (top panel), which presents a similar slope change for the first point. To quantify the deviation of the first ATLAS detection from the early behaviour of the LC, we fit a parabola to the ATLAS flux density (expressed in μJy) assuming a flux scaling $F \propto t^2$ (e. g. Riess et al. 1999; Conley et al. 2006). Under this assumption, the first ATLAS point is ~ 0.7 mags brighter than the predicted LC. However, the early r - and ATLAS o -filter detection limits (see Figs. 2, 3) exclude the occurrence of a pre-maximum bump (as in Leloudas et al. 2012; Nicholl et al. 2015b; Smith et al. 2016) up to ~ 53 rest-frame days before the estimated explosion epoch. However, we note that the post-maximum epochs ATLAS o -filter data fluctuate within ~ 0.25 mag in a timescale $\lesssim 10$ days. Also, they do not apparently show up in other filters. This allows for a 0.25 mag maximum uncertainty for ATLAS magnitudes, which is much less than the 0.7 mag deviation for the first point, making the flat start more credible. Finally, the K -corrected and S-corrected $uvw2, uvm2, uvw1, u, U, B, g, V, r, i, z, J, H, K_s, W1, W2$ host-template subtracted photometry of SN 2018hti was combined to obtain the pseudo-bolometric LC displayed in Fig. 4 (data are listed in Tab. A12). This was computed by integrating the multiband photometry neglecting every flux contribution out of the integration boundaries. For SN 2018hti, the epochs of the r -band photometry are adopted as reference. The extinction corrected combined fluxes were finally converted to pseudo-bolometric luminosities by multiplying by $4\pi d_L^2$. Similar to the multiband LCs, the pseudo-bolometric LC has a ratio $\tau_{\text{decline}}/\tau_{\text{rise}} \sim 1.8$ (similar to other SLSNe I, see e. g. Nicholl et al. 2015a).

⁶ Obtained via the NASA/IPAC Extragalactic Database https://ned.ipac.caltech.edu/extinction_calculator.

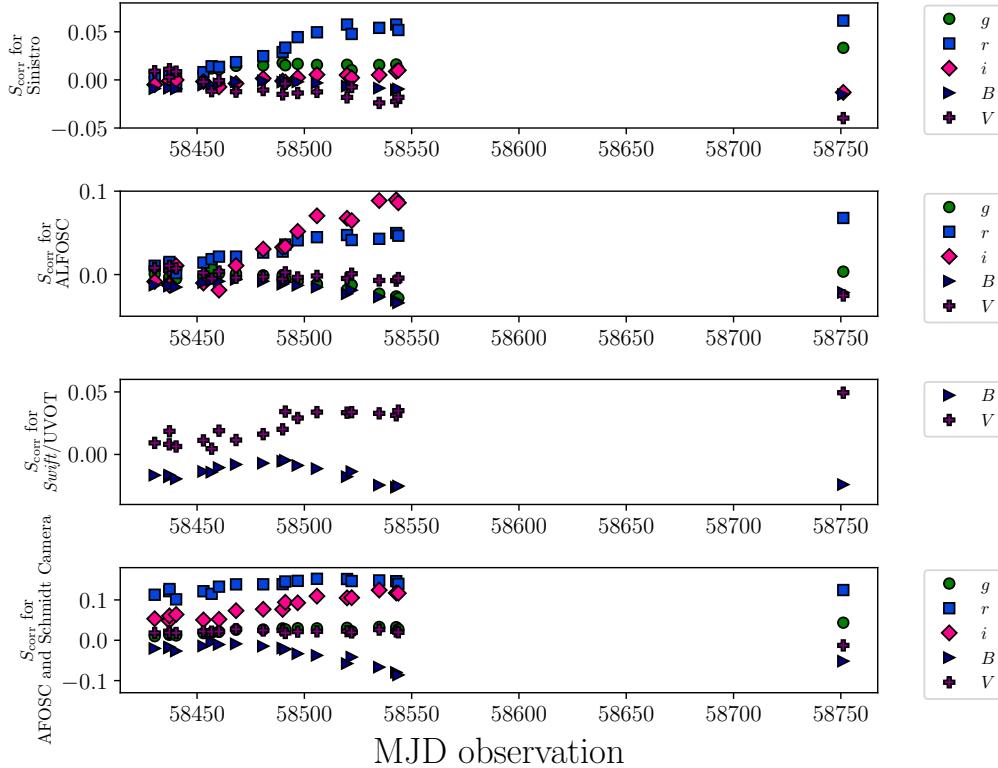


Figure 1. S-correction in B , V , g , r , i -filter passbands for different instruments (Sinistro, ALFOSC, *Swift*/UVOT, AFOSC/Schmidt Camera, in descending order).

3 SPECTROSCOPY

3.1 Observations and data reduction

We collected a dense sample of spectra for SN 2018hti starting from MJD = 58 430.2 (2018 November 8), which corresponds to 32 rest-frame days before maximum light.

We led the spectroscopic follow up via the extended/advanced Public ESO Spectroscopic Survey for Transient Objects (Smartt et al. 2015) (ePESSTO/ePESSTO+), NUTS/NUTS2, with the 1.82-m Copernico telescope at the Asiago astrophysical observatory, Italy, the 2.4m Hiltner Telescope+OSMOS (Ohio State Multi-Object Spectrograph) at the Michigan-Dartmouth-MIT Observatory and the Hobby Eberly Telescope (HET)+LRS2 (Low Resolution Spectrograph) at the McDonald observatory, Texas. Moreover, we took a pre-maximum (-18 rest-frame days) NIR spectrum via the 3.0-m NASA Infrared Telescope Facility (IRTF)+SpeX (Rayner et al. 2003) and a nebular spectrum on 2019 September 24 (+269 rest-frame days) with the 10.4m Gran Telescopio CANARIAS (GTC)+OSIRIS (Optical System for Imaging and low-Intermediate-Resolution Integrated Spectroscopy, Cepa et al. 2000) at Roque de los Muchachos Observatory. Additional FLOYDS spectra were obtained from FLOYDS on the Faulkes Telescope South (or North) as part of the Global Supernova Project. The instrumental setups and the resolution of the spectra presented in this work are listed in Tab. A13.

The AFOSC, EFOSC2 and GTC spectra were reduced with the standard `IRAF` procedures. Firstly, the raw bidimensional spectroscopic frames were debiased, flatfielded and corrected for the cosmic-rays contribution with the Laplacian Cosmic Ray Identification package (`LACOSMIC`, van Dokkum 2001). Then the spectra were ex-

tracted along the spatial direction with the `IRAF` task `APALL` after having subtracted the background contribution, which was estimated via a low-order polynomial fit. The one-dimensional spectra were wavelength calibrated against HeAr (for the NTT+EFOSC2), HeNe (for NOT+ALFOSC spectra), NeHgCd (for the 1.82m-Copernico+AFOSC spectra) and HgArNe (for GTC+OSIRIS spectrum) calibration arcs. Then the extracted one-dimensional spectra were flux calibrated via a set of spectrophotometric standard stars observed on the same night and with the same instrumental setup as the science observations. Using the flux-calibrated standard star spectrum we were able to remove the contribution of the telluric absorption features. Finally, the flux calibration was checked against co-eval photometry. The ALFOSC spectra were reduced with `FOSCGUI`⁷. The OSMOS spectrum was reduced with the `PYRAF`-based `SIMSPEC`⁸ pipeline. The LRS2 spectra were reduced with a dedicated `IRAF`- and `PYTHON`-based pipeline (as in Yang et al. 2020, see Sec. 2.2.3). FLOYDS spectra were reduced using the `FLOYDSSPEC` pipeline⁹. The IRTF+SpeX spectrum was reduced utilizing the `SPEXTOOL` software package (Cushing et al. 2004).

⁷ `FOSCGUI` is a graphic user interface aimed at extracting SN spectroscopy and photometry obtained with FOSC-like instruments. It was developed by E. Cappellaro. A package description can be found at <http://sngroup.oapd.inaf.it/fosogui.html>.

⁸ <https://astro.subhashbose.com/simspec/>.

⁹ https://github.com/svalenti/FLOYDS_pipeline/blob/master/bin/floydsspec/

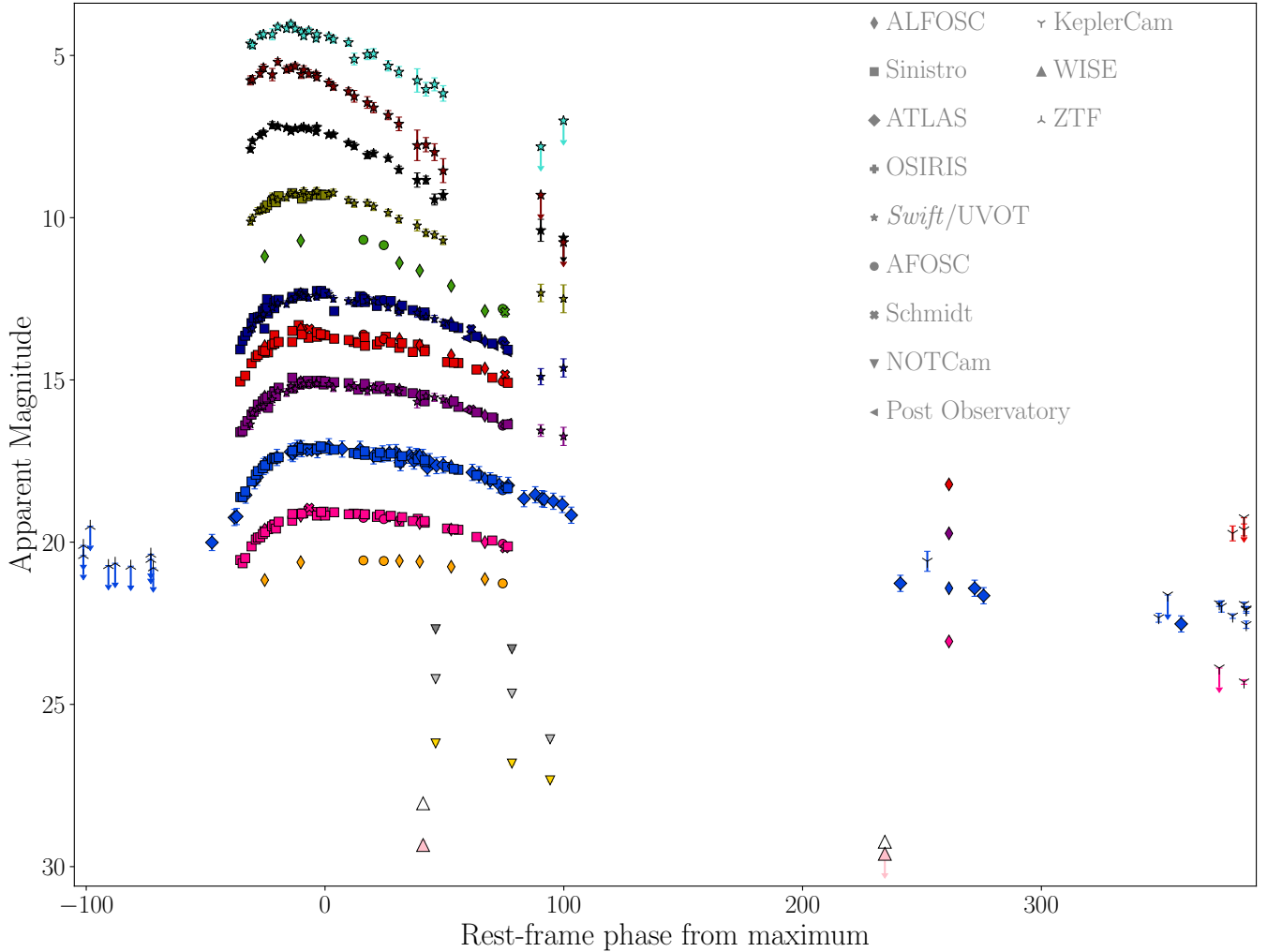


Figure 2. $uvw2$, $uvm2$, $uvw1$, U , u , B , g , V , r , i , z , J , H , K_s , $W1$, $W2$ observed LCs of SN 2018hti, respectively plotted in brown, cyan, black, dark green, dark blue, green, blue, red, purple, magenta, orange, silver, yellow, white and pink. Data obtained with different instruments are plotted with different markers, as labelled in the top-right corner. Magnitudes are plotted in ABmags.

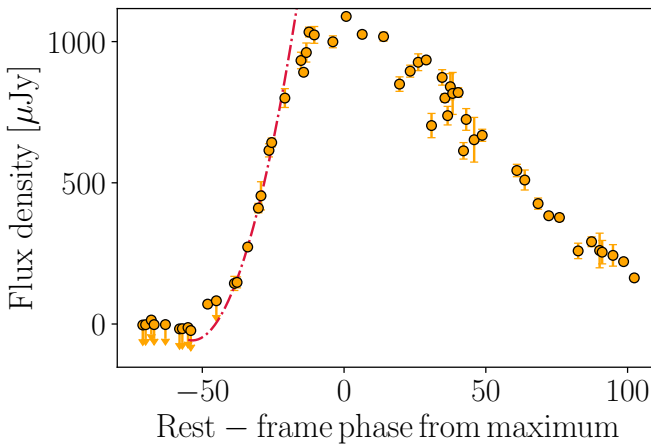


Figure 3. ATLAS- α LCs of SN 2018hti (yellow dots) in flux space (expressed in μJy). The early ATLAS LC is fitted with a second-order polynomial (dashed dotted red line).

3.2 Spectral evolution and line identifications

The spectral evolution of SN 2018hti is shown in Fig. 5. Throughout their evolution, the spectra of SN 2018hti show $\text{H}\beta$, $\text{H}\alpha$, $[\text{O III}]\lambda 4959$, $[\text{O III}]\lambda 5007$ narrow emission lines from the host galaxy, which we use to measure the redshift of the host galaxy and to estimate the metallicity at the site of SN 2018hti (see Sect. 4.1).

The pre-maximum/maximum-light spectra of SN 2018hti present a very hot continuum reaching blackbody temperatures of $\sim 18000 - 22000$ K. They show the W-shaped O II absorptions between 3500–5000 Å. In addition, from the earliest spectrum at phase -34 days from the maximum light, a broad feature ($\text{FWHM} \sim 15000 - 18000 \text{ km s}^{-1}$) starts to rise in a nearly boxy fashion (see Sec. 4.5.1). We interpreted this feature as $\text{C II} \lambda 6580$ (as in Nicholl et al. 2014, see also the discussion in Sec. 4.5.1). We also mention that the TARDIS modelling of a sample of more than 180 spectra of SLSNe I predicts a $\text{C II} 6584.70$ at a fraction above 50% with a small contribution of $\text{Ne I} \lambda\lambda 6404.02, 6508.83$ (Paraskeva et al. in prep). This feature does not however reproduce a boxy profile. The early NIR spectrum of SN 2018hti (see Fig. 6) shows an almost featureless continuum with the exception of an emission at a rest-frame wavelength about \simeq

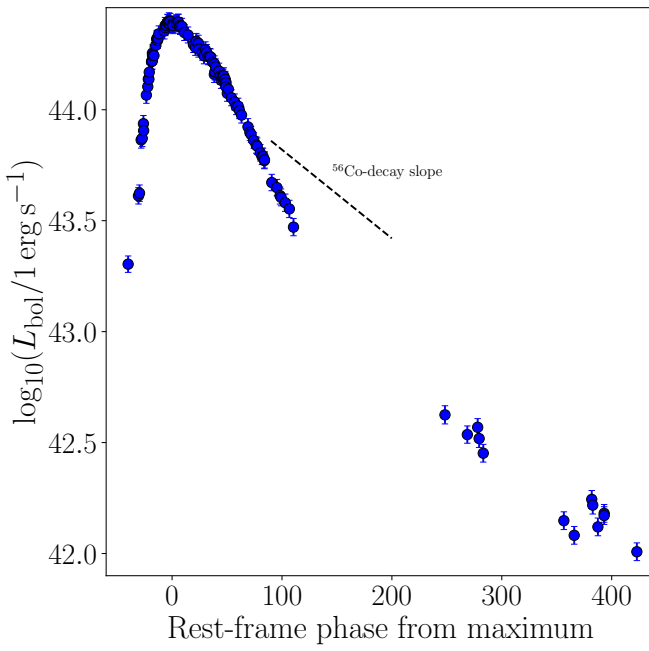


Figure 4. Pseudo-bolometric LC of SN 2018hti (blue dots). The black-dashed line indicates the slope of ^{56}Co -decay.

9200 Å which we interpreted as $\text{C II} \lambda 9234$, similar to the cases of Gaia16apd (Yan et al. 2017a) and to SN 2015bn (Nicholl et al. 2016).

In the spectrum taken 4 days after maximum light, the Fe II emission features are visible in the blue regions, while Mg II begins to be seen in the 15 day post-maximum spectrum. On the same epoch, $\text{O I} \lambda 7774$ appears in the red end of the spectrum. About 15–30 days after maximum light, the spectrum of SN 2018hti smoothly enters the SN Ic/SNe Ic BL-like phase, similarly to many other SLSNe I (e.g. Pastorello et al. 2010; Inserra et al. 2013; Gal-Yam 2019a). After 39 rest-frame days from maximum an emission shows up at ~ 6360 Å, which we interpreted as $\text{Si II} \lambda 6355$. In the 52 day post-maximum spectrum the $\text{Ca II NIR} \lambda\lambda\lambda 8498, 8542, 8662$ triplet becomes visible. After SN 2018hti reappeared from behind the sun, we took the GTC+OSIRIS spectrum on 2019 September 24, 269 days after maximum light. This spectrum is not completely nebular as it displays some residual continuum, which could be however influenced by a residual contribution from the host galaxy (see also Jerkstrand et al. 2017). This phase was referred to as ‘pseudo-nebular’ by Nicholl et al. (2019).

4 DISCUSSION

Here we discuss the data presented above. Where possible, we compare data of SN 2018hti with those of other SLSNe I. To do this, we selected a sample of SLSNe I which share some spectro-photometric properties with those of SN 2018hti. We included LSQ14bdq (Nicholl et al. 2015b), SN 2006oz (Leloudas et al. 2012) and DES14X3taz (Smith et al. 2016) since their r -filter LCs show a pre-maximum bump. Moreover, SN 2015bn (Nicholl et al. 2016) was prompted as the best-spectral match by GELATO (Harutyunyan et al. 2008). The SLSNe I iPTF13ehe, iPTF15esb and iPTF16bad

(Yan et al. 2015, 2017b) were added to the comparison sample since they show $\text{H}\alpha$, although at later epochs with respect to maximum light. Finally, we added also a late spectrum of Gaia16apd (Kangas et al. 2017) since few SLSNe I spectra are available at pseudo-nebular/nebular phases.

4.1 Metallicity at the location of SN 2018hti

As mentioned earlier, SLSNe I usually explode in metal-poor, star-forming environments. Several metallicity diagnostics are calibrated from the emission lines emerging from the host-galaxy spectrum. In the case of SN 2018hti, we measured the flux emitted by the $[\text{O II}] \lambda 3727$, $\text{H}\beta$, $[\text{O III}] \lambda 4959$, $[\text{O III}] \lambda 5007$, $\text{H}\alpha$ and $[\text{S II}] \lambda 6717$ narrow emission lines emerging from the host galaxy in the nebular spectrum. To measure the flux emitted within the narrow emission lines, we extracted the host-galaxy spectrum close to the position of SN 2018hti by placing the aperture adjacent to the SN itself.

One of these indicators is referred to as R_{23} (Pagel et al. 1979):

$$R_{23} = \frac{([\text{O II}] \lambda 3727 + [\text{O III}] \lambda 4959, 5007)}{\text{H}\beta}. \quad (1)$$

Another indicator which is often used is the so-called N2O2 (Kewley & Dopita 2002):

$$\text{N2O2} = \frac{[\text{N II}] \lambda 6584}{[\text{O II}] \lambda 3727}. \quad (2)$$

For SN 2018hti we found $\log_{10} R_{23} = 0.96$ and $\log_{10}(\text{N2O2}) = -1.26$. To measure the metallicity of the host galaxy at the site of SN 2018hti, we evaluated different metallicity estimators simultaneously thanks to the tool PYMCZ¹⁰ presented by Bianco et al. (2016). PYMCZ randomly samples a Gaussian distribution whose mean and standard deviation are given by the flux measurements and their uncertainties, respectively. With this tool, it was possible to exploit the d04 (Denicoló et al. 2002), m91 (McGaugh 1991), m08_N2H_A, m08_o3o2 (Maiolino et al. 2008) and m13_N2 (Marino et al. 2013) metallicity estimators. Other metallicity estimators calculated by PYMCZ are excluded from our analysis since they are not suitable for the case of SN 2018hti. In particular, z94 (Zaritsky et al. 1994) is valid only for the upper branch of the $\log_{10} R_{23}$ scale¹¹. Also, the kd02 and kk04 methods should only be used for $\log_{10}(\text{N2O2}) > -1.2$. The results are shown in the boxplot in Fig. 7 and are summarized in Tab. 1. As expected, the results point towards a metal-poor site with $12 + \log_{10}(\text{O/H}) \approx 8.17$, which corresponds to a metallicity $Z \approx 0.3 Z_\odot$ (assuming $12 + \log_{10}(\text{O/H}) = 8.69$ for the solar metallicity, Asplund et al. 2009). This estimate nicely agrees with the results obtained by Lin et al. (2020a). Moreover, we estimated the star formation rate (SFR) of the host galaxy of SN 2018hti based on the measurements of the flux emitted by the reddening corrected narrow $\text{H}\alpha$ using equation 2 of Kennicutt (1998). The derived SFR is $\sim 0.3 M_\odot \text{ yr}^{-1}$, similar to the SFRs measured by Chen et al. (2017a) for a sample of galaxies hosting SLSNe I and comparable to the SFR of the Large Magellanic Cloud (Harris & Zaritsky 2009). Finally, we compared the values of SFR and metallicity of SN 2018hti with those of the comparison sample (see Tab. 2). Given the intrinsic uncertainty of these measurements, the selected SLSN-I sample seem to share similar environments, with the exception of SN 2015bn, which has a SFR about an order of magnitude lower than the others. However,

¹⁰ The package can be found at <https://github.com/nyusngroup/pyMCZ>.

¹¹ The upper-branch metallicity scale is defined by the condition $\log_{10} R_{23} < 0.9$ (e.g. Kewley & Ellison 2008).

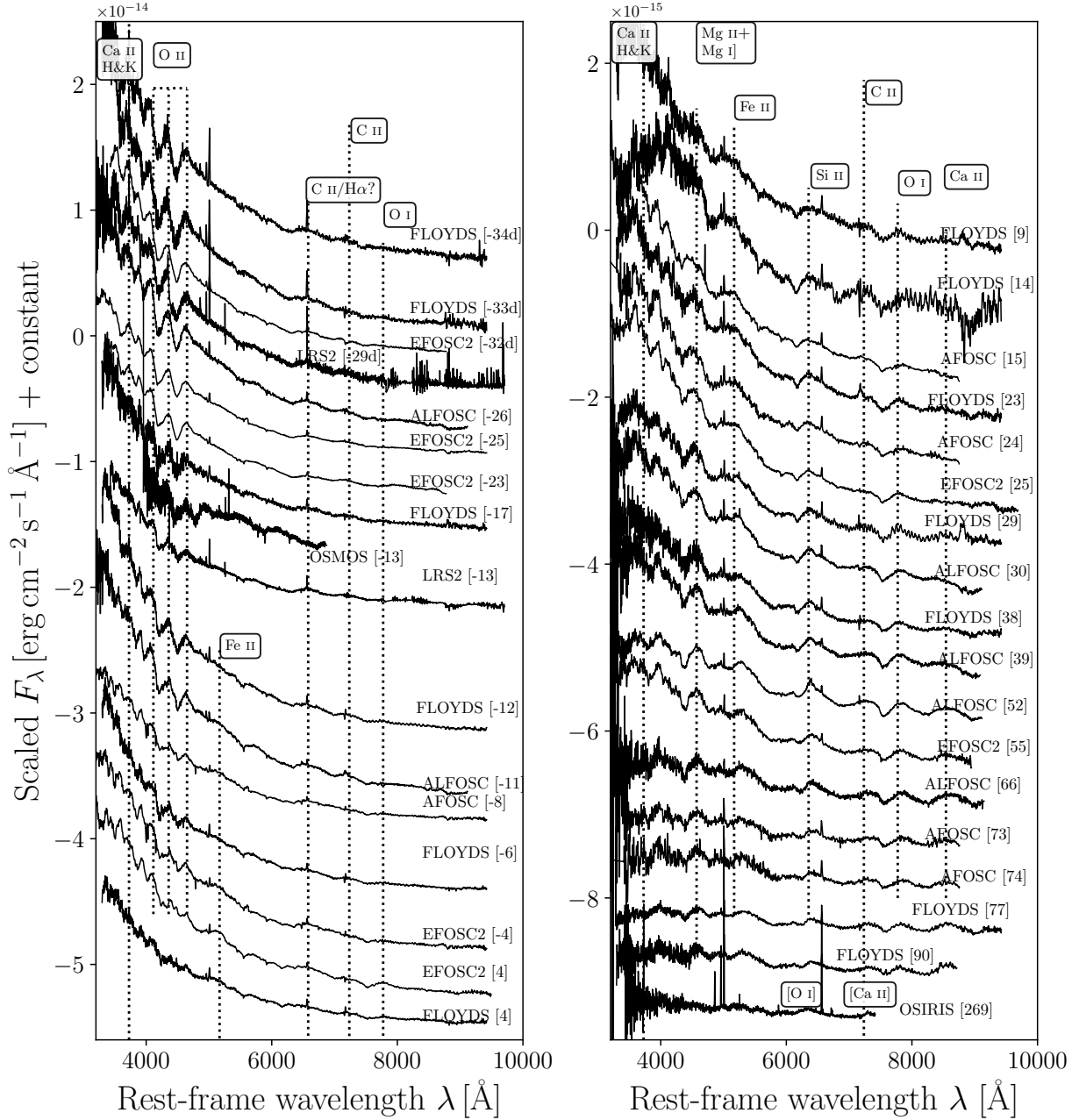


Figure 5. Spectral evolution of SN 2018hti. Spectral line identifications are marked with vertical black dotted lines, and labelled on its right side with the corresponding ion. The rest-frame phase with respect to maximum luminosity is reported on the right side of each spectrum. The left panel shows the spectral evolution of SN 2018hti from -34 days to 4 days from maximum luminosity and the right panel shows the remaining spectra up to 269 days after maximum luminosity.

as pointed out by [Nicholl et al. \(2015b\)](#), modelling the host-galaxy SED and estimating the median stellar mass and the age of the stellar population returns a higher SFR value of $0.55 \pm 0.18 M_{\odot} \text{ yr}^{-1}$ for SN 2015bn. Also, the SFR value reported for LSQ14bdq is a SFR limit (see also Sec. 4 in [Chen et al. 2017a](#)).

4.2 Blackbody temperature and photospheric radius

We obtained the time evolution of the blackbody temperatures by fitting a blackbody curve to the spectra. This allows us to avoid the contribution of the spectral lines in the fitting procedure by excluding the line-contaminated regions from the fit domain. The comparison of the temperature evolution of SN 2018hti with SN 2015bn ([Nicholl et al. 2016](#)), SN 2006oz ([Leloudas et al. 2012](#)), iPTF13ehe ([Yan et al. 2015, 2017b](#)), iPTF15esb ([Yan et al. 2017b](#)), iPTF16bad ([Yan et al. 2017b](#)) is shown in Fig. 8 (left panel). The data of SN 2006oz

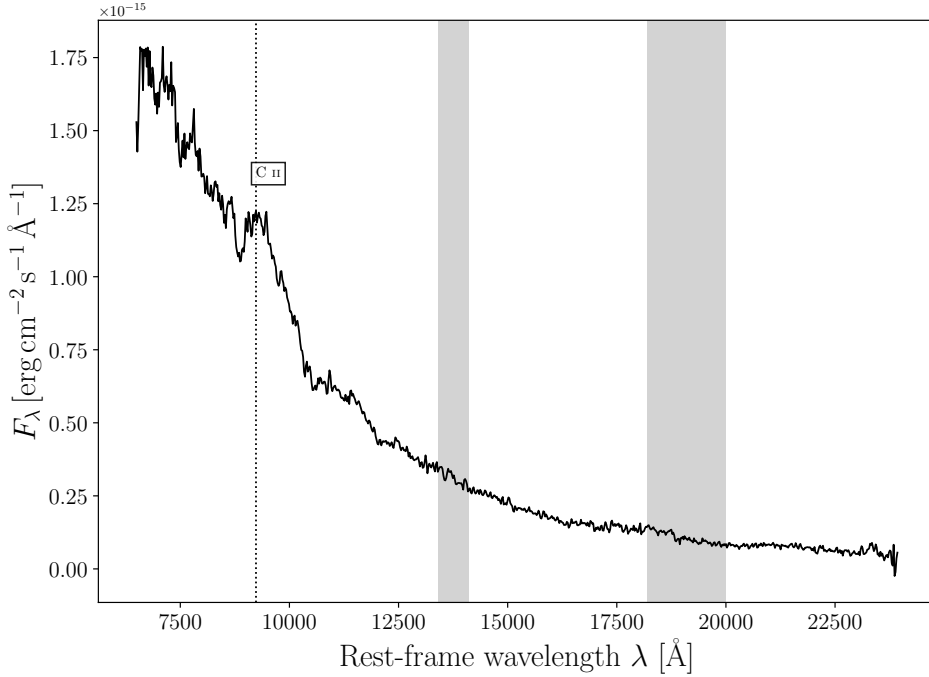


Figure 6. The IRTF+SpeX spectrum of SN 2018hti (black solid line). The black dotted line marks the C II at $\lambda = 9234 \text{ \AA}$ line identification and the shaded gray areas mark the spectral regions corrected for telluric absorptions.

estimator	$12 + \log_{10}(\text{O/H})$
d02	$8.128^{+0.142}_{-0.149}$
m91	$8.214^{+0.123}_{-0.055}$
m08_N2HA	$8.215^{+0.013}_{-0.013}$
m08_o3o2	$8.156^{+0.033}_{-0.033}$
m13_N2	$8.113^{+0.044}_{-0.042}$

Table 1. Metallicity estimators provided by the PYMCZ tool for the site of SN 2018hti (see also Fig. 7).

are relatively dispersed, but are useful for an order-of-magnitude comparison. The temperature evolution of SN 2018hti is essentially monotonic and is very similar to the case of SN 2006oz, the steepest of the sample. SN 2018hti and SN 2006oz appear to have the hottest photospheres among the SLSNe I sample. However, the scarcer sampling of the blackbody temperatures of iPTF13ehe and iPTF16bad do not allow to properly compare them with SN 2018hti. In particular, both SN 2015bn and iPTF15esb reach a ‘temperature floor’ (Nicholl et al. 2017b) of $5000 - 8000 \text{ K}$ after $\sim 50 - 80$ days after maximum luminosity (Fig. 8) similar to the sample analysed by Inserra et al. (2013) (see also Nicholl et al. 2017b). In the case of SN 2018hti it is unclear whether or not the temperature evolution actually settles on a plateau at that phase.

We also determine the evolution of the photospheric radius (Fig. 8, right panel) R_{ph} using the Stefan-Boltzmann law, where we used the pseudo-bolometric luminosities shown in Fig. 4. To compare the more sparsely sampled spectroscopic epochs with those of the pseudo-bolometric luminosities, we fit the blackbody temperatures with a second-order polynomial. The photospheric ra-

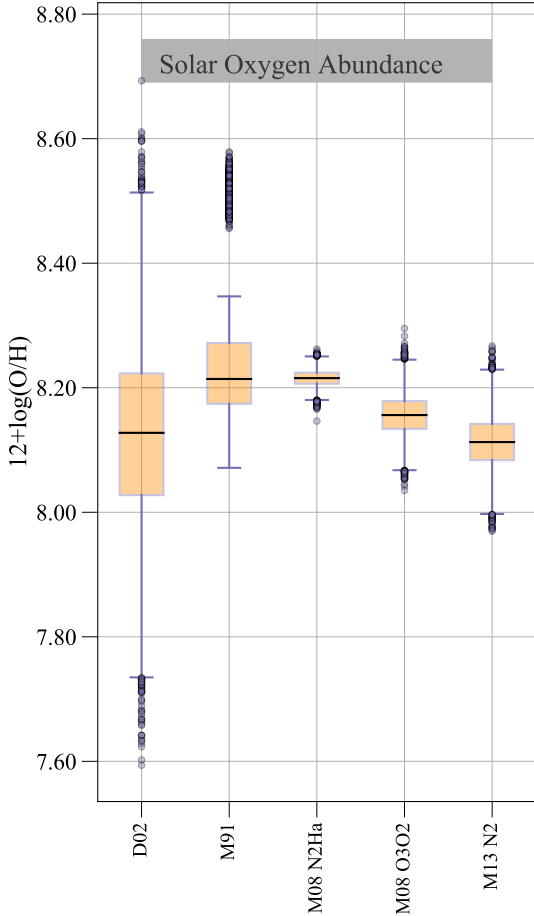
dius of SN 2018hti monotonically grows to a maximum value of $\sim 9 \times 10^{15} \text{ cm}$ in 100 days, which is about ~ 50 days later the maximum bolometric luminosity. It then recedes at a rate of about $7 \times 10^{13} \text{ cm}^2 \text{ day}^{-1}$, which is similar to the average growth rate. Overall, the photospheric-radius evolution is consistent with the expansion radius determined from expansion velocity derived from some spectral lines (see Sec. 4.3) except for the time interval between -26 and 35 rest-frame days from maximum (see Fig. 8, right panel). However, given the huge uncertainties, this should be considered only as an order-of-magnitude comparison. In the same figure we also show the photospheric-radius evolution of SN 2006oz. The photosphere of SN 2006oz seems less extended than that of SN 2018hti. In fact, given that both of them have a comparable photospheric temperature, SN 2006oz is about ~ 0.5 mag fainter than SN 2018hti (see Fig. 11).

4.3 Photospheric velocity

The photospheric velocity of SN 2018hti is measured via the O II $\lambda 4357$, O II $\lambda 4650$ and O I $\lambda 7774$ P-Cygni absorption features present in the spectra. In particular, it has been shown that the O I $\lambda 7774$ feature is a good tracer of the photosphere of the stripped envelope SNe (Dessart et al. 2015). The wavelengths corresponding to the absorption minima were inferred from a Gaussian fit of the absorption features (see Fig. 9). This method is marginally affected by the line blending (Jeffery & Branch 1990) which can substantially bias the velocity measurements (Gal-Yam 2019b). The velocity evolution of SN 2018hti is shown in Fig. 10 (right panel) in comparison with the photospheric velocities of SN 2015bn, iPTF13ehe, iPTF15esb and iPTF16bad (where the photospheric velocities of iPTF13ehe, iPTF15esb and iPTF16bad were retrieved based on the Fe II $\lambda 5169$). In the case of SN 2018hti, after an initial very steep decline, the veloc-

Table 2. Metallicities and SFRs of the SLSNe I of the comparison sample as published in literature.

SN 2018hti	LSQ14bdq	SN 2015bn	SN 2006oz	DES14X3taz
Z/Z_{\odot}	0.3	-	0.2 (Nicholl et al. 2016)	0.5 (Leloudas et al. 2012)
SFR [$M_{\odot} \text{ yr}^{-1}$]	0.3	<0.05 (Chen et al. 2017a)	0.04 (Nicholl et al. 2016)	0.17 (Leloudas et al. 2012)
				0.16 (Smith et al. 2016)

**Figure 7.** Boxplot obtained with the tool PYMCZ. The orange boxes cover the interquartile range (IQR) for each estimator, and the blue dots deviate from the first and third quartile more than $1.5 \times \text{IQR}$. The gray box broadly corresponds to the solar oxygen abundance.

ity evolution settles on an early plateau which starts ~ 22 days before maximum luminosity and lasts ~ 30 days. Overall, the photosphere of SN 2018hti recedes (in mass coordinates) similarly to SN 2015bn and both of them are much slower than the other SLSNe I of the comparison sample. Finally, we compared the photospheric-velocity evolution of SN 2018hti with the results of the numerical radiation hydrodynamic calculations of Kasen & Bildsten (2010, see also their Fig. 2, bottom panel) for a magnetar-powered SN assuming a magnetic field $B_p = 0.5 \times 10^{14}$ G, an initial period $P_{\text{spin}} = 5$ ms, an ejecta mass $M_{\text{ejecta}} = 5 M_{\odot}$ and a kinetic energy $E_{\text{kin}} = 10^{51}$ erg. We scaled this solution by a factor 1.37 to almost perfectly fit the measured photospheric velocities of SN 2018hti (see also Sec. 4.5.2).

4.4 Comparisons with other SLSNe I

We compared the r -filter absolute magnitude LC of SN 2018hti with those of the comparison sample (see Fig. 11, left panel). These SLSNe I show an early bump in their LCs and/or spectral signatures that likely involve some ejecta-CSM interaction (i.e. a possible H α emergence). Interestingly, this sample shares similar evolutionary timescales (see Fig. 11, left panel) up to ~ 80 days after maximum light, even though the absolute peak magnitude spans a range > 2 mag.

Three representative spectra of SN 2018hti (at phases -8, +73, +269 days after maximum) are compared with the spectra of LSQ14bdq, SN 2018bsz, DES14X3taz, Gaia16apd and SN 2015bn (Fig. 12). The spectra of LSQ14bdq, 2018bsz, iPTF15esb, Gaia16apd, DES14X3taz and SN 2015bn are from WISEREP¹² (Yaron & Gal-Yam 2012). The spectrum of SN 2018hti taken 8 days prior to maximum light is compared with the spectra of LSQ14bdq (at a phase of -15 rest-frame days), SN 2018bsz (at a phase of -6 rest-frame days) and DES14X3taz (at a phase of -21 rest-frame days). At these phases, the O II features in the blue region of the spectrum of SN 2018hti nicely match those of LSQ14bdq, SN 2018bsz and DES14X3taz. However, in the earliest spectrum of SN 2018bsz the P-Cygni maximum of the O II $\lambda 4650$ feature is likely affected by line blending with C II $\lambda 4745$ (Anderson et al. 2018). At about 60-70 days after maximum luminosity, the spectrum of SN 2018hti is also similar to the spectrum of iPTF15esb, although the latter shows a more prominent Mg I $\lambda 4571$ and broader Fe-group features at ~ 5500 Å. The remarkable resemblance between SN 2018hti and SN 2015bn at about 70 days after maximum suggests that these SNe have similar ejecta velocities (see also Fig. 10) and chemical composition. Finally, the late/pseudo-nebular spectrum of SN 2018hti at 269 days after maximum is compared with the spectra of SN 2015bn and Gaia16apd at a phase +270 days and +252 days, respectively. The nebular emission features of SN 2015bn and Gaia16apd are more strongly developed compared to SN 2018hti, although they share some resemblance in the blue region of the spectrum.

4.5 Data interpretation

We considered two different scenarios to interpret the data of SN 2018hti: the magnetar and the ejecta-CSM interaction scenarios. To test the viability of the two hypotheses we modelled the multi-colour LCs of SN 2018hti with the Modular Open Source Fitter for Transients (MOSFIT, Guillochon et al. 2017, 2018). We also used the published radiative-transfer solutions of the SUMO code (Jerkstrand et al. 2017) for the nebular emission of O-zone material in SLSNe I (see Sec. 4.5.3) as a guide for the interpretation of the pseudo-nebular spectrum of SN 2018hti. This allows us to constrain the mass of the progenitor of SN 2018hti.

¹² <https://wiserep.weizmann.ac.il>.

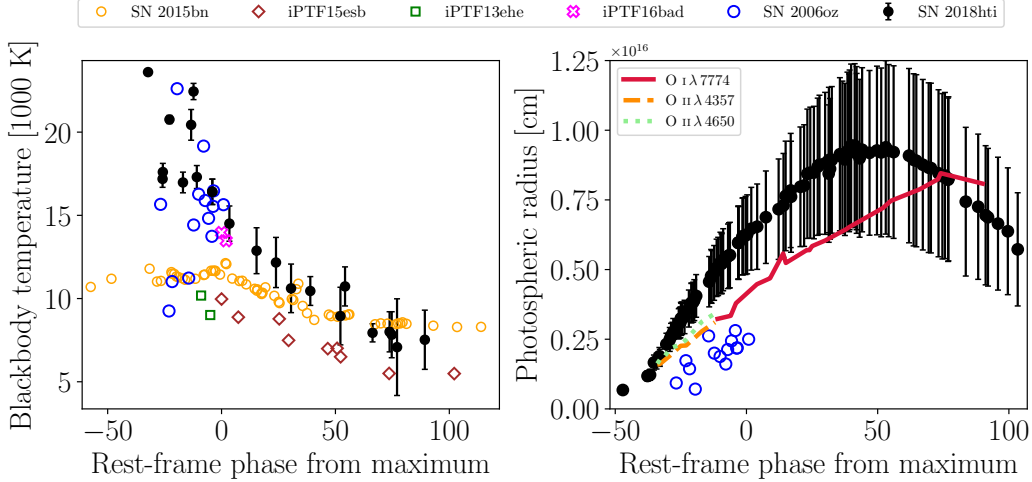


Figure 8. Left panel: the blackbody temperatures of SN 2018hti (black filled dots). The blackbody temperature evolution of SN 2015bn (orange empty dots, Nicholl et al. 2016), SN 2006oz (blue empty dots, Leloudas et al. 2012), iPTF13ehe (green empty squares, Yan et al. 2015, 2017b), iPTF15esb (brown empty diamonds, Yan et al. 2017b) and iPTF16bad (magenta empty crosses, Yan et al. 2017b) are also shown for comparison. Right panel: the evolution of the photospheric radius of SN 2018hti (black dots) compared with SN 2006oz. For comparison we also plot the radius obtained from the photospheric-velocity measurements performed on the spectra for the O I (red solid line) and the O II absorptions ($\lambda 4357$, orange dashed line, $\lambda 4650$, green dotted line).

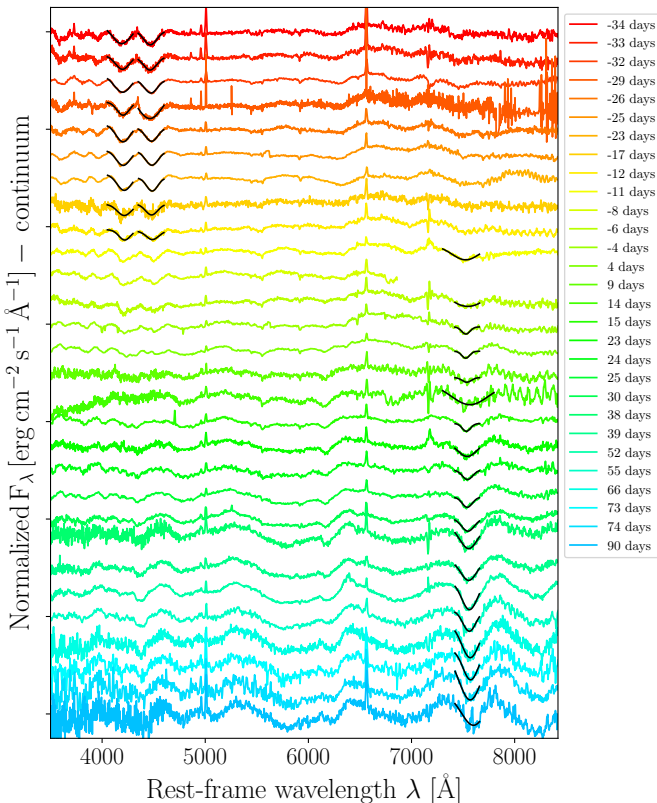


Figure 9. Normalized and continuum-subtracted spectra of SN 2018hti. A gaussian curve (black solid line) is fitted to the absorption minima of the O II $\lambda\lambda 4357, 4650$ and the O I $\lambda 7774$ features. For the epochs in which more than one spectrum is available, we chose the spectrum with the greatest signal-to-noise ratio.

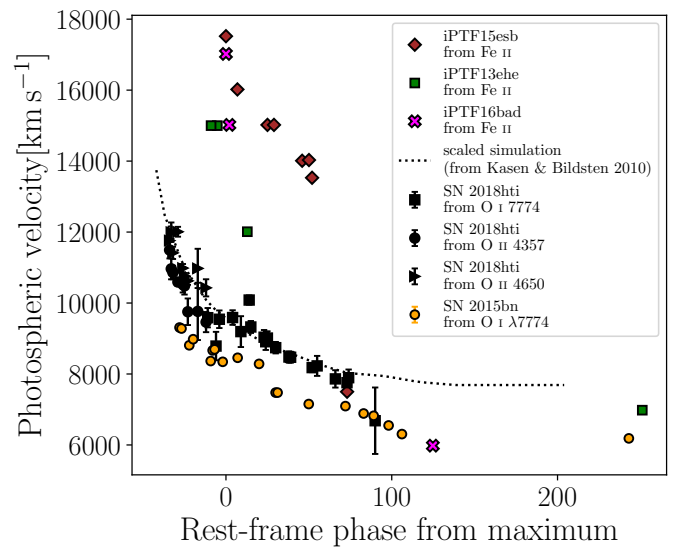


Figure 10. Photospheric velocities of SN 2018hti deduced from the absorption minima of O II $\lambda\lambda 4357, 4650$ (black dots and triangles) and O I $\lambda 7774$ (black squares) P-Cygni profiles (see text). The evolution of the photospheric velocity of SN 2015bn (deduced by the O I, data taken from Nicholl et al. 2016, yellow dots), iPTF13ehe (green squares), iPTF15esb (brown diamonds), iPTF16bad (magenta crosses) (deduced by the Fe II, Yan et al. 2017b) are shown for comparison. We also compared the photospheric velocity of SN 2018hti with the prediction of Kasen & Bildsten (2010) for a magnetar-powered SN (black dotted line, see text).

4.5.1 The early boxy feature

The flat-topped line profile of the emission feature at $\sim 6500 \text{ \AA}$ could be suitably explained by emission inside an expanding shell of matter (Weiler 2003; Jerkstrand 2017). The identification of this feature is not straightforward, and could be attributed either to H α or to C II $\lambda 6580$. To investigate this line identification, we superimpose on top

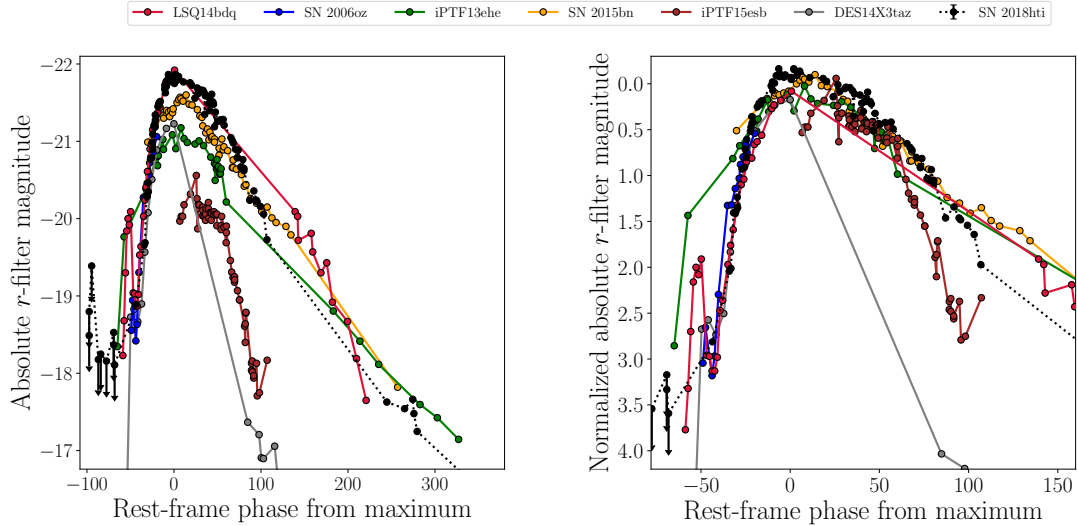


Figure 11. Left panel: comparison of the *r*-filter absolute magnitude LC of SN 2018hti with those of LSQ14bdq (red dots), SN 2006oz (blue dots), iPTF13ehe (green dots), SN 2015bn (yellow dots), iPTF15esb (brown dots) and DES14X3taz (gray dots). Right panel: same as the left panel, but with the LCs normalized to maximum luminosity. Absolute magnitudes were corrected for Galactic extinction as in Sec. 2 and calculated with the assumed cosmology in this work. Where K -correction values were not available, we assume a constant K -correction $2.5 \log(1+z)$.

of the boxy feature the line profiles of the possible H β (where a tiny bump is present, see Fig. 13) and of C II λ 9234 (see Fig. 14). The comparison between the H α and H β spectral regions is arduous because the H β region is also potentially contaminated by other spectral features (such as O II and Fe II). On the other hand, the boxy line is well reproduced by the C II λ 9234 feature in the IRTF+SpeX spectrum, suggesting that their flat profiles stem from the same matter shell and thus favouring a C II λ 6580 identification. Detailed radiative transfer calculations (e. g. Dessart et al. 2012; Dessart 2019) actually predict the presence of the C II λ 6580 feature in the SLSNe I spectra, but do not predict the boxy shape for the C II λ 6580. This suggests that the models may need to more carefully account for dynamical effects such as the formation of a thick shell, which is expected from both from magnetar and CSM interaction scenario.

4.5.2 Light curves fits with MOSFIT

MOSFIT includes a number of models for different kinds of astronomical transients. In particular, those suitable for the SLSNe I are the csm (CSM interaction powered), csmni (CSM interaction + ^{56}Ni -decay powered), the sasn and the MAGNETAR (two implementations of the magnetar powered case, see later) and the MAGNI (magnetar+ ^{56}Ni -decay powered) models. We chose the sasn and the csm modules to fit the photometry of SN 2018hti, which respectively exploit the models introduced by Inserra et al. (2013) and Chatzopoulos et al. (2012). Since MOSFIT takes as input the multiband LCs, it has to rebuild the pseudo-bolometric luminosities once a SED model has been assumed. We chose the sasn model since it accounts for the UV blanketing assuming an absorbed-blackbody model for the SED computation. We excluded the $W1, W2$ magnitudes from the fit procedure since the MIR part of the SED could deviate from a single blackbody component at epochs which are not covered by our photometric dataset.

Also, the sasn model includes constraints ensuring the energy conservation and that the ejecta do not become optically thin before 100 days after maximum, as not to contradict the late spectroscopic observations of the SLSNe (see Sec. 3.8 in Nicholl et al. 2017b).

The results of the fit procedures are shown in Fig. 15, 16 and the corner plots showing the best-fit parameters are shown in Fig. 17, 18. The sasn fit supports a magnetar engine with a polar magnetic field of $\sim 1.3 \times 10^{13}$ G and an initial period of ~ 1.8 ms, for an ejecta mass $M_{\text{ej}} \approx 5.3 M_{\odot}$ (see Fig. 17), opacity $\kappa \approx 0.1 \text{ cm}^2 \text{ g}^{-1}$, gamma-ray opacity $\kappa_{\gamma} \approx 0.02 \text{ cm}^2 \text{ g}^{-1}$, an average ejecta velocity $v_{\text{ej}} \approx 8500 \text{ km s}^{-1}$ and a temperature floor $T_{\min} \approx 9300 \pm 250$ K. This corresponds to a kinetic energy $E_{\text{kin}} = 3.7 \times 10^{51}$ erg. These results are absolutely reasonable for what is expected by the magnetar scenario for SLSNe I (e. g. Nicholl et al. 2017b) and are in perfect agreement with the estimates of Lin et al. (2020a). Except for the ejecta mass, the best-fit parameters for the magnetar case are quite different from those assumed in the calculations of Kasen & Bildsten (2010). This difference could possibly explain the need of the scaling factor 1.37 that we used in Sec. 4.3 to match the predicted photospheric velocity with the observed one. Moreover, the value of the kinetic energies required by both interpretations largely overcomes the maximum explosion energy that can be provided by a neutrino-driven mechanism during the core collapse (Soker & Gilkis 2017; Kaplan & Soker 2020). This energy budget might require the contribution of jets in the explosion of SN 2018hti. However, its negligible polarization degree (Lee 2019) suggests that its explosion was nearly spherical, thus making this hypothesis less likely.

The csm fit of SN 2018hti instead requires the interaction of the SN ejecta with a mass of $\sim 8.3 M_{\odot}$ and average velocity $v_{\text{ej}} \approx 1.1 \times 10^4 \text{ km s}^{-1}$ with a CSM mass $M_{\text{CSM}} \approx 10.5 M_{\odot}$ and average density $\rho \approx 4.1 \times 10^{-13} \text{ g cm}^{-3}$. This corresponds to a kinetic energy $E_{\text{kin}} = 1.1 \times 10^{52}$ erg. Also, for this model the predicted temperature floor reached by SN 2018hti is $T_{\min} \approx 9500 \pm 180$ K. Both the predictions of T_{\min} can be considered in agreement with what was deduced in Sec. 4.2. The best-fit slope of the CSM density profile $s \sim 0.2$ seemingly favours a shell-like CSM with nearly-constant density (Chatzopoulos et al. 2013). The CSM interaction scenario may be disfavoured because of the absence of narrow/multicomponent features in the spectra (typical e.g. of SNe IIn) and because there was no significant detection in X-ray (see Sec. 2).

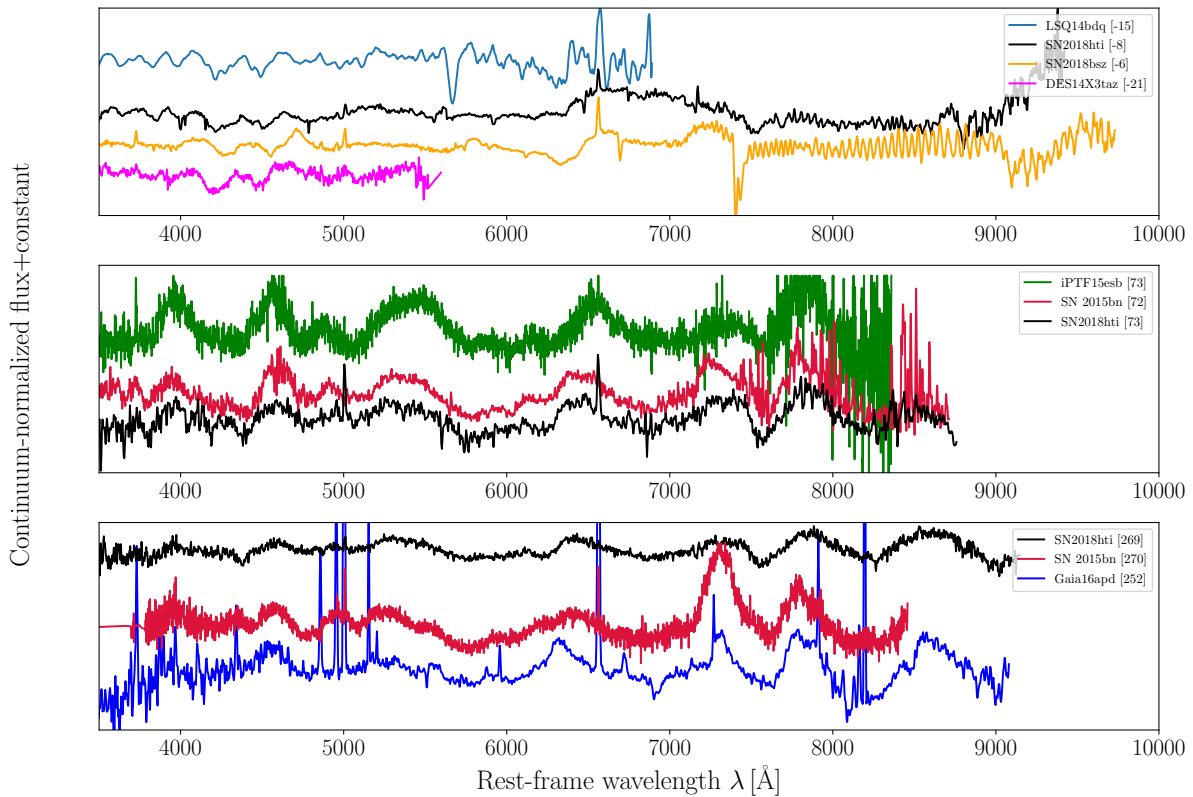


Figure 12. Comparisons of three spectra of SN 2018hti at different phases with respect to maximum luminosity (the rest-frame phase from maximum luminosity is indicated among square brackets in the legend). Upper panel: comparison among SN 2018hti (8 days before maximum, black line), SN 2018bsz (13 days before maximum, Anderson et al. 2018), LSQ14bdq (15 days before maximum, light blue line, see Nicholl et al. 2015b) and DES14X3taz (21 rest-frame days before maximum, magenta line, Smith et al. 2016). Middle panel: comparison among SN 2018hti (73 rest-frame days after maximum, black line), SN 2015bn (72 rest-frame days after maximum, red line) and iPTF15esb (73 rest-frame days from maximum, green line, see Yan et al. 2017b). Lower panel: comparison between SN 2018hti (269 rest-frame days after maximum, black line), SN 2015bn (270 rest-frame days after maximum, red line, see Nicholl et al. 2016) and Gaia16apd (252 rest-frame days after maximum, blue line, Kangas et al. 2017). For a better visualization, the spectrum of LSQ14bdq was smoothed with a Savitzki-Golay filter due to its lower signal-to-noise ratio. The spectra of iPTF15esb, 2018bsz, LSQ14bdq, SN 2015bn and of Gaia16apd were obtained via WISEREP.

However, these arguments cannot rule out the CSM-interaction scenario for SN 2018hti if the CSM is highly asymmetric, e. g. if it has a disc-like geometry. In fact, if the CSM is not seen perfectly edge on, the optically thick ejecta may form a photosphere outside the CSM so that the ejecta CSM interaction takes place underneath it and the X-ray, UV photons can be reprocessed by further radiation-matter interactions (as it was proposed by Andrews & Smith 2018, for the peculiar SN II iPTF14hls).

4.5.3 Interpretation of the nebular spectrum

The nebular spectrum of SN 2018hti taken 269 rest-frame days after maximum light was interpreted with SUMO modelling (Jerkstrand et al. 2017). The best-matching SUMO models are built with a C-burning composition, $M_{\text{ejecta}} = 30 M_{\odot}$, a filling factor $f = 0.001$, an energy deposition $E_{\text{dep}} = 10^{42} \text{ erg s}^{-1}$ and a pure-O abundance $M_{\text{ejecta}} = 10 M_{\odot}$, $f = 0.1$, $E_{\text{dep}} = 2 \times 10^{42} \text{ erg s}^{-1}$. In the following, we will refer to them as C30 and O10 respectively. They are shown in Fig. 19 with the pseudo-nebular spectrum of SN 2018hti.

In particular, O10 better reproduces the bluer region of the spectrum (until $\sim 5200 \text{ \AA}$, see Fig. 19) whereas C30 better matches the redder region. Also, the best-matching spectra permit identification of other broad features in the spectrum, such as $[\text{O III}] \lambda\lambda 4959, 5007$, $\text{Mg I } \lambda 5180 + [\text{Fe II}] \lambda 5250$ and $[\text{O I}] \lambda 5577$. We estimated the progenitor mass of SN 2018hti by measuring the flux emitted within the $\text{O I } \lambda 7774$ emission feature predicted by C30 using equations (7) and (8) of Jerkstrand et al. (2017). The choice of C30 is motivated by the fact that it better describes the Oxygen features in the spectrum, as the $[\text{O I}] \lambda\lambda 6300, 6364$ and $[\text{O I}] \lambda 5577$ features. The flux integrated within the $\text{O I } \lambda 7774$ feature gives $L_{7774} = 2.25 \times 10^{40} \text{ erg s}^{-1}$. Hence we assumed $f = 0.001$, the Oxygen mean molecular weight $\bar{A} = 16$, an electron fraction $x_e = 0.1$ (Jerkstrand et al. 2017, see their Sec. 4.2.1), a maximum expansion velocity $V = 8000 \text{ km s}^{-1}$ (we adopted for V a value consistent with the velocity plateau at late times, see Fig. 10) and a recombination coefficient $\alpha^{\text{eff}}(T) = 2 \times 10^{-13} \text{ cm}^3 \text{ s}^{-1}$. Solving equation (7) of Jerkstrand et al. (2017) for the electron density n_e , this gives $n_e \sim 1.28 \times 10^9 \text{ cm}^{-3}$. Using this value in equation (8) in Jerkstrand et al. (2017), the O-zone mass is estimated to

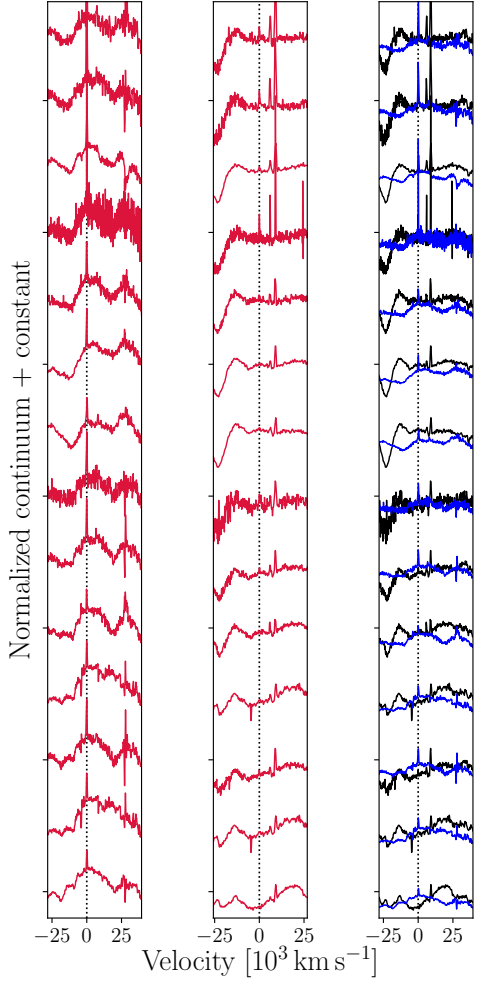


Figure 13. Left panel: a close up of the $H\alpha$ region in the early spectral evolution of SN 2018hti (red solid lines). Central panel: same as in the left panel, but for the $H\beta$ region. Right panel: overlap of the $H\alpha$ (blue solid lines) and $H\beta$ (black solid lines) regions, where the $H\alpha$ region was superposed to that of $H\beta$. The dotted vertical black lines mark the rest-frame wavelength of $H\beta$ (middle panel) and of $H\alpha$ (left and right panel). The rest-frame phases of the spectra are labelled on the right side of the right panel.

Table 3. Comparison of the ejecta masses of the best-matching SUMO solutions with MOSFIT best-fit parameters.

ejecta mass [M_\odot]	
SUMO	10-30
MOSFIT CSM	8.32
MOSFIT SLSN	5.25

be $M_{\text{O-zone}} \approx 6.2 M_\odot$, which according to more recent models of stellar evolution of a single star corresponds to a progenitor mass $M_{\text{ZAMS}} \approx 40 M_\odot$ (Jerkstrand et al. 2017). Similar consideration can be made for the O10 solution (corresponding to $f = 0.1$ and $x_e \approx 0.5$), which predicts a O-zone mass $M_{\text{O-zone}} \approx 10 M_\odot$ (for this solution we require $V \lesssim 7000 \text{ km s}^{-1}$ in order not to obtain $M_{\text{O-zone}} > M_{\text{ejecta}}$). In the latter case, the ejecta is expected to be much Mg-poorer compared to the C30 case. Another reason to favour the C30 model lies in its ejecta clump density. In fact, C30 is 300

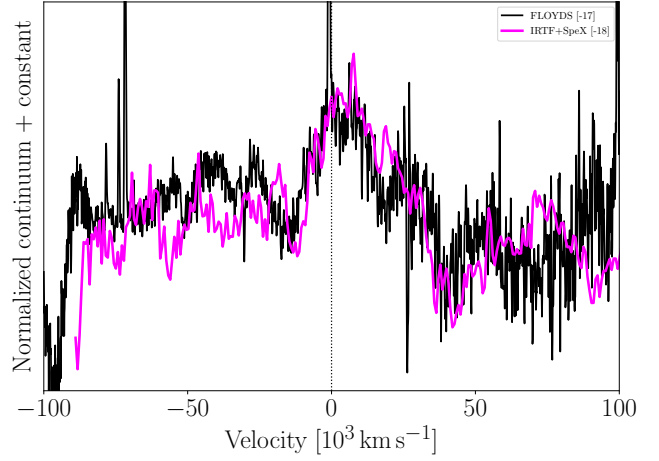


Figure 14. Comparison between the continuum-normalized FLOYDS (black line) and IRTF+SpeX (magenta line) spectra of SN 2018hti at comparable phases. The optical and the NIR spectra are plotted in velocity coordinates with respect to $\lambda = 6580 \text{ \AA}$ and $\lambda = 9234 \text{ \AA}$, respectively.

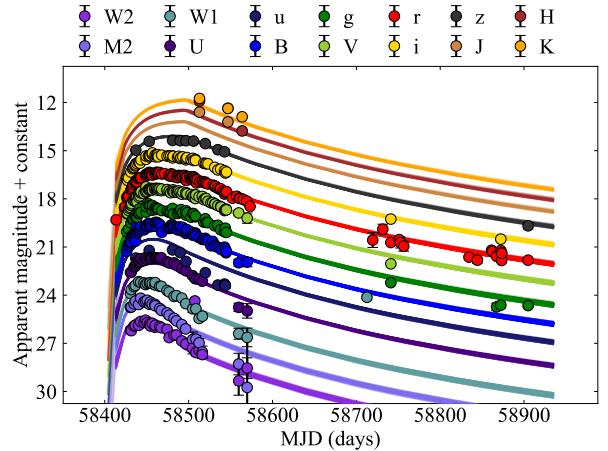


Figure 15. Best-fit MOSFIT synthetic LCs to the multiband photometry of SN 2018hti obtained with the SLSN model.

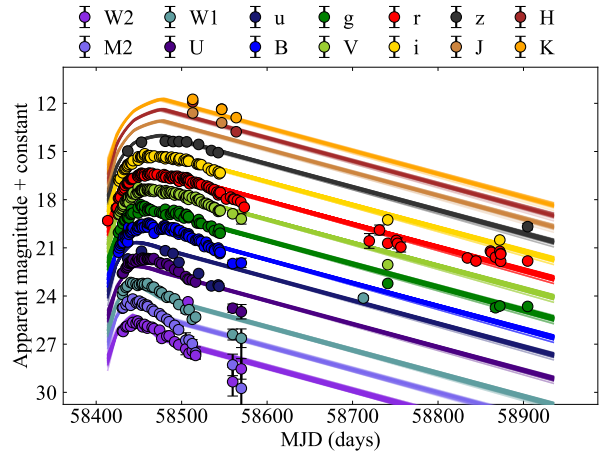


Figure 16. Same as in Fig. 15, but for the csm model.

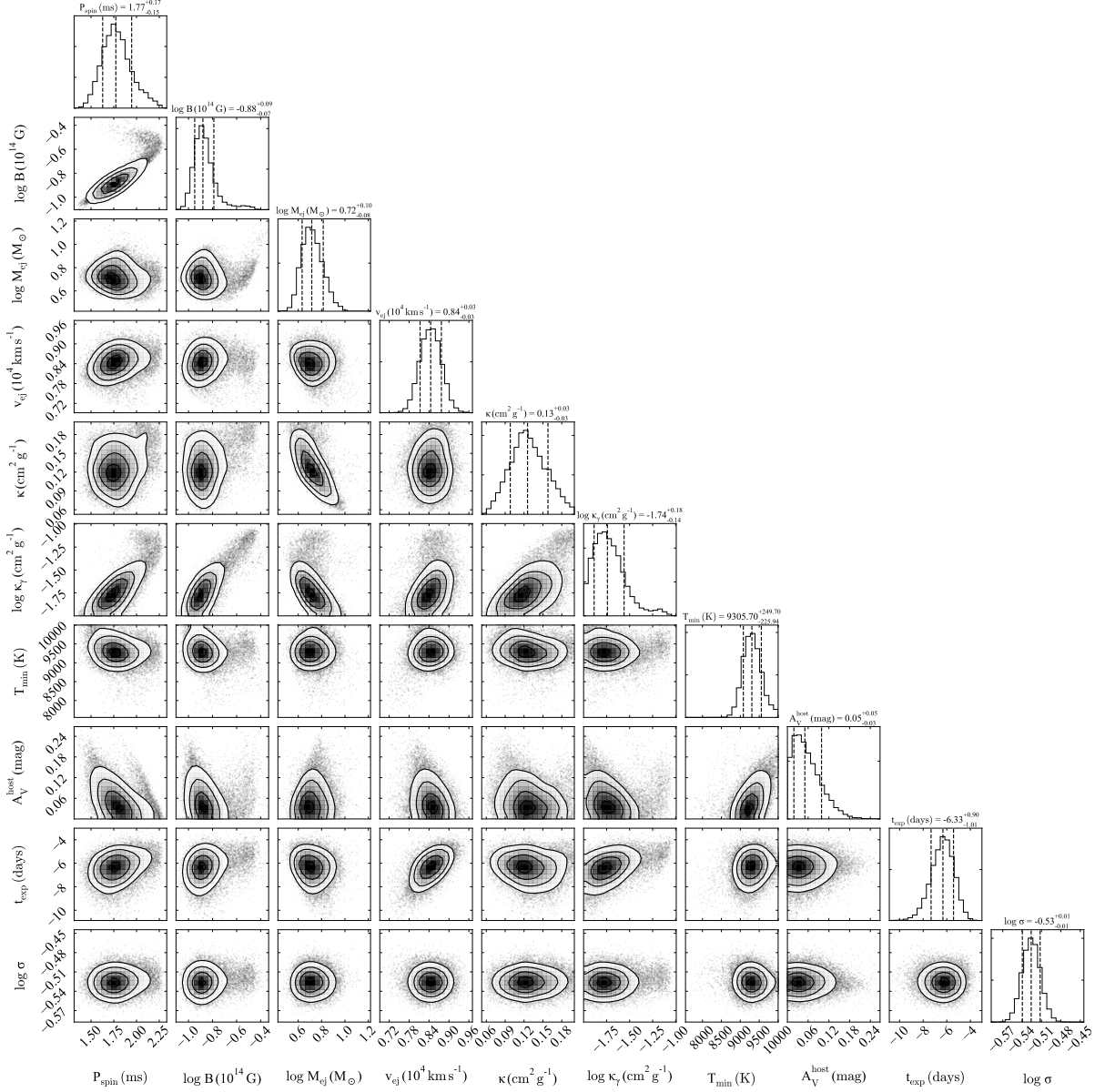


Figure 17. Corner plot with the best-fit parameters of the MOSFIT fit obtained with the sLSN model.

times denser than O10¹³. This could be also the reason why no strong [O I] λ 6300 and [Ca II] + [O II] λ 7300 emission is seen in the nebular spectrum, as it would emerge for higher-density models.

Finally, in Tab. 3 we summarized the ejecta-mass estimates obtained with the MOSFIT fits and the SUMO nebular modelling. The SUMO O10 solution apparently favours the CSM model since the ejecta mass used by O10 nearly reproduces that one estimated by the MOSFIT CSM fit, whereas the MOSFIT SLSN fit predicts an ejecta mass which is pretty lower than what is suggested by the SUMO solutions. However, we warn the reader that the (single-zone) SUMO solutions are computed for a phase of 400 days post-explosion, which is not the case for the pseudo-nebular spectrum of SN 2018hti. Hence, the

¹³ The factor 300 comes from $(30 \text{ M}_\odot / f_{C30}) / (10 \text{ M}_\odot / f_{O10}) = 300$, where $f_{C30} = 0.001$ and $f_{O10} = 0.1$ are the clumping factors for the models C30 and O10, respectively.

density in the model is by a factor $(400/270)^3 \simeq 3.3$ lower than the corresponding case at 270 days. This biases a direct constrain on the ejecta density and mass. In addition, it is hard to believe that in the case of SN 2018hti the CSM interaction is acting as its major power source even if we interpret the modest C II boxy feature as a signature of the interaction with a CSM dense shell. According to the MOSFIT CSM fit, the predicted CSM mass is $\sim 10.5 \text{ M}_\odot$. We expect that the interaction with a similar amount of mass of CSM would cause strong spectral emissions as in the case of the type IIn SN 2008iy (Chugai 2021) and SN 2010jl (Ofek et al. 2014). However, as we mentioned earlier, a disk-like and dense CSM can hide the spectral signatures of CSM-interaction. Based on this considerations, we argue that the mechanism powering SN 2018hti could be either the spindown radiation from a millisecond magnetar with $B_p \sim 1.3 \times 10^{13}$ G and $P_{\text{spin}} \sim 1.8$ ms or the (buried) interaction of the ejecta with $\sim 10 \text{ M}_\odot$ of a disk-like CSM.

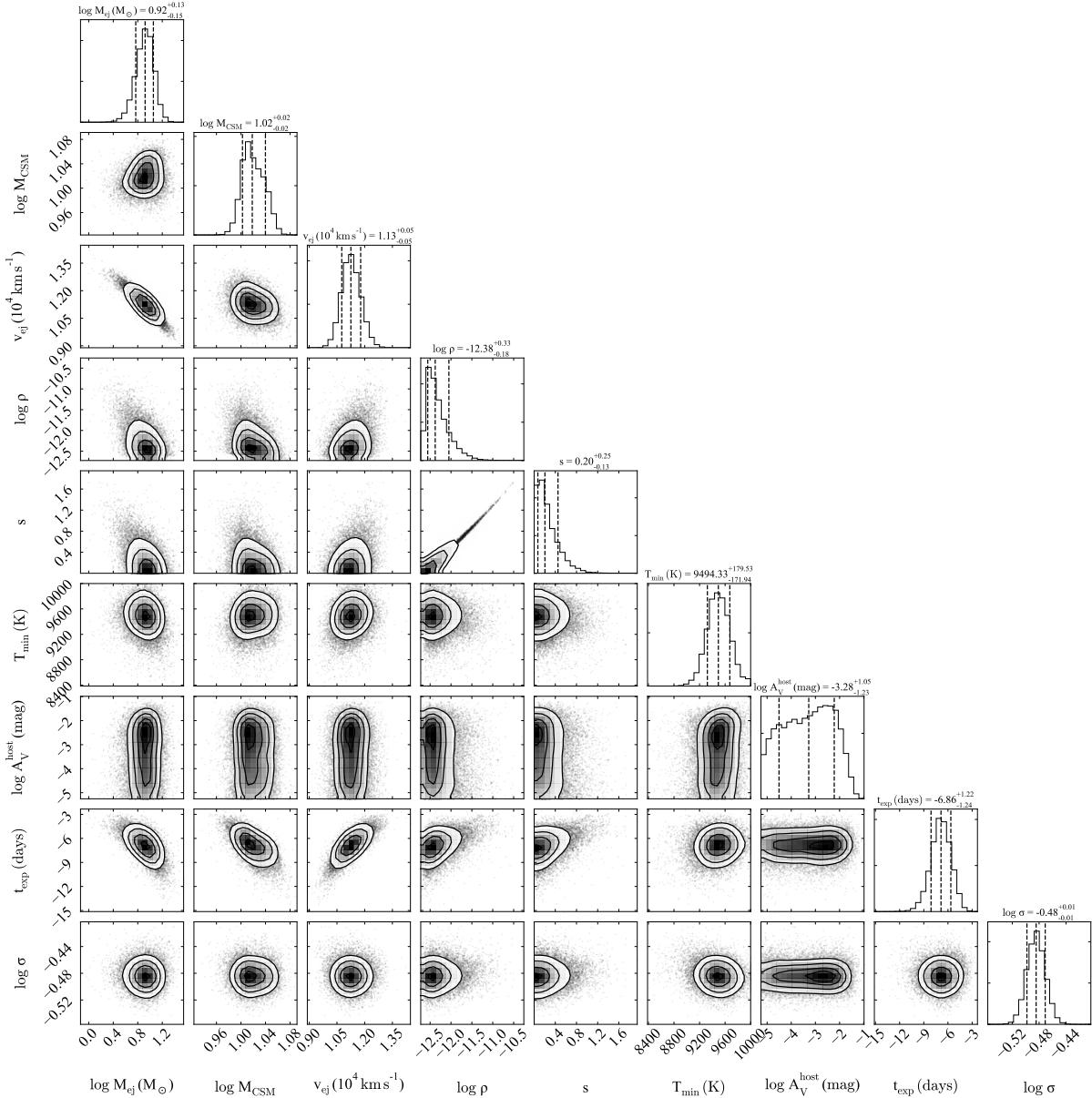


Figure 18. Same as Fig. 17 but for the csm model.

5 CONCLUSIONS

In this work, we have presented the UV/optical/NIR photometry and the NIR/optical spectroscopy of the SLSN I SN 2018hti. It slowly rose for ~ 50 days towards a peak absolute magnitude of ~ -21.7 mag in the r -band. Alongside this slow rise and extremely high luminosity, the presence of the prominent O II absorptions in the pre-maximum/maximum spectra identifies this object as a (slow-evolving) SLSN I. In the H α region, the early spectra show a flat-topped feature which we interpret as H α . C-rich SLSNe I spectra are predicted by magnetar- and a pair-instability driven radiative transfer calculations (Dessart et al. 2012; Dessart 2019), but the boxy profile suggests that the feature could originate from the shock mediated interaction of the SN ejecta with a surrounding CSM. In addition, metallicity measurements via the host narrow emission lines are aligned with the low-metallicity paradigm of SLSNe I. Finally, we estimated the physical parameters of the explosion, both in the

magnetar and in the CSM-interaction scenarios, fitting synthetic LCs to the multicolor photometry of SN 2018hti with the MOSFiT tool. The model fits suggest that either interaction of a $8 M_\odot$ SN ejecta with $\sim 10 M_\odot$ of CSM or the spindown radiation of a $B \sim 1.3 \times 10^{13}$ G, $P_{\text{spin}} \sim 1.8$ ms magnetar could be the major power source for SN 2018hti.

We interpret the pseudo-nebulosity spectrum of SN 2018hti with synthetic spectra published by Jerkstrand et al. (2017) for a SN Ic. We concluded that, assuming a single-star progenitor scenario for SN2018hti, the progenitor ZAMS mass was of $\sim 40 M_\odot$. These findings help to unravel the origin of the complexities that often appear in SLSNe-I LCs (e.g. Inserra et al. 2017), finding a reasonable explanation in CSM-ejecta interaction. This sheds light on the nature of SLSNe I progenitors.

The advent of the new generation, wide-field surveys such as the Legacy Survey of Space and Time at the Vera Rubin Observatory will

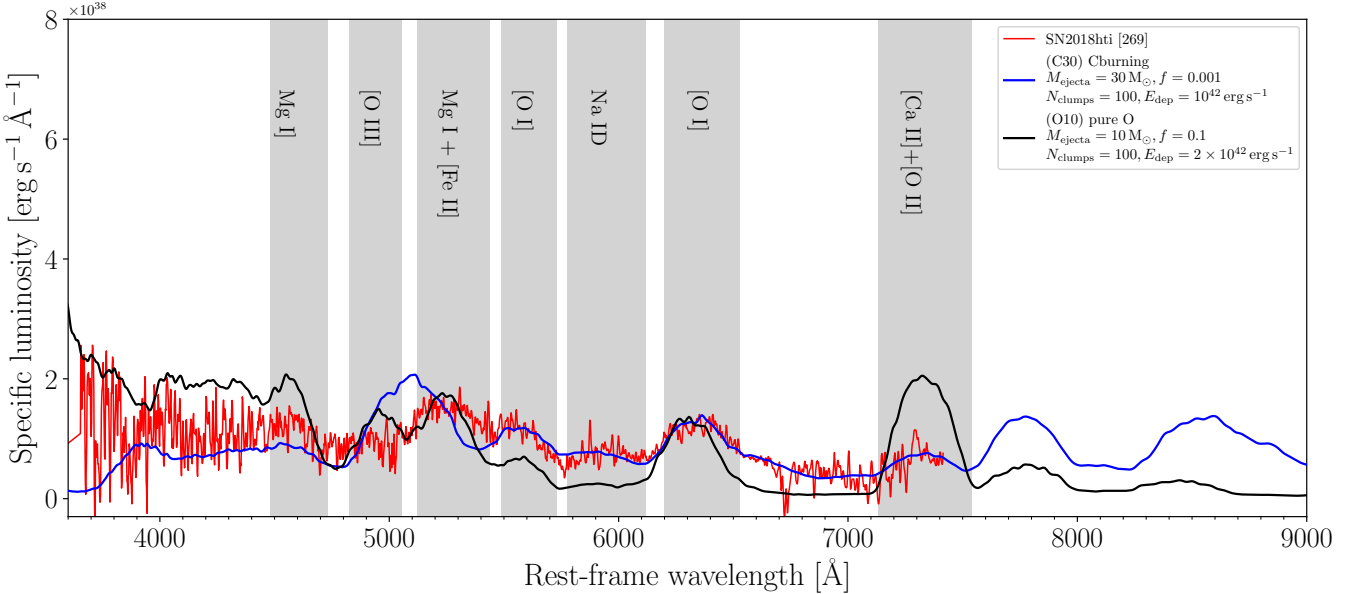


Figure 19. Comparison of the GTC+OSIRIS nebular spectrum (red line) with two outputs of the SUMO numerical code (see text) for a full C-ashes model (blue line) and a pure-O composition (black line).

contribute to broaden our knowledge about the SLSN astrophysics (Villar et al. 2018).

ACKNOWLEDGEMENTS

We thank the anonymous referee for her/his valuable comments which improved the present work. AF acknowledges Stephen Smartt, Marica Branchesi, Noam Soker and Morgan Fraser for their suggestions and for interesting discussions. This work is based on observations made with the Nordic Optical Telescope, owned in collaboration by the University of Turku and Aarhus University, and operated jointly by Aarhus University, the University of Turku and the University of Oslo, representing Denmark, Finland and Norway, the University of Iceland and Stockholm University at the Observatorio del Roque de los Muchachos, La Palma, Spain, of the Instituto de Astrofísica de Canarias. The data presented here were obtained in part with ALFOSC, which is provided by the Instituto de Astrofísica de Andalucía (IAA) under a joint agreement with the University of Copenhagen and NOT. Based on observations collected at Copérnico and Schmidt telescopes (Asiago, Italy) of the INAF - Osservatorio Astronomico di Padova. MG is supported by the EU Horizon 2020 research and innovation programme under grant agreement No 101004719. M.S. acknowledges the Infrared Telescope Facility, which is operated by the University of Hawaii under contract 80HQTR19D0030 with the National Aeronautics and Space Administration. N.E.R. acknowledges support from MIUR, PRIN 2017 (grant 20179ZF5KS). TMB was funded by the CONICYT PFCHA /DOCTORADO BECAS CHILE/2017-72180113. AJ acknowledges funding from the European Research Council (ERC) under the European Union's Horizon 2020 Research and Innovation Program (ERC Starting Grant. AR acknowledges support from ANID BECAS/DOCTORADO NACIONAL 21202412. Y.-Z. Cai is funded by China Postdoctoral Science Foundation (grant no. 2021M691821). T.-W.C. acknowledges the EU Funding under Marie Skłodowska-Curie grant H2020-MSCA-IF-2018-842471. KM is funded by the

EU H2020 ERC grant no. 758638. G. P. is supported by ANID - Millennium Science Initiative - ICN12_009. We thank the staff at the different observatories for performing the observations. Based on observations collected at the European organisation for astronomical research in the Southern Hemisphere, Chile, as part of ePESSTO+ (the advanced Public ESO Spectroscopic Survey for Transient Objects). ePESSTO+ observations were obtained under ESO program id 199.D-0143 (PI: Inserra). Based on observations made with the Gran Telescopio Canarias (GTC), installed in the Spanish Observatorio del Roque de los Muchachos of the Instituto de Astrofísica de Canarias, in the island of La Palma. This work makes use of observations from the Las Cumbres Observatory network. The LCO team is supported by NSF grants AST-1911225 and AST-1911151.

DATA AVAILABILITY STATEMENT

The data presented in this paper and listed in Appendix A are available in the online supplementary material. The spectra will be made public via WISEREP.

REFERENCES

- Agnoletto I., et al., 2009, *ApJ*, **691**, 1348
- Anderson J. P., 2019, *A&A*, **628**, A7
- Anderson J. P., et al., 2018, *A&A*, **620**, A67
- Andrews J. E., Smith N., 2018, *MNRAS*, **477**, 74
- Angus C. R., et al., 2019, *MNRAS*, **487**, 2215
- Asplund M., Grevesse N., Sauval A. J., Scott P., 2009, *ARA&A*, **47**, 481
- Becker A., 2015, HOTPANTS: High Order Transform of PSF AND Template Subtraction (ascl:1504.004)
- Bhirombhakdi K., Chornock R., Miller A. A., Filippenko A. V., Cenko S. B., Smith N., 2019, *MNRAS*, **488**, 3783
- Bianco F. B., Modjaz M., Oh S. M., Fierroz D., Liu Y. Q., Kewley L., Graur O., 2016, *Astronomy and Computing*, **16**, 54
- Blanchard P. K., Nicholl M., Berger E., Chornock R., Milisavljevic D., Margutti R., Gomez S., 2019, *ApJ*, **872**, 90

- Brown T. M., et al., 2013, *PASP*, **125**, 1031
- Burke J., Hiramatsum D., Arcavi I., Howell D. A., McCully C., Valenti S., 2018, Transient Name Server Classification Report, [2018-1719](#), 1
- Cappellaro E., 2014, SNOOPY: a package for SN photometry, <http://sngroup.oapd.inaf.it/snoopy.html>
- Cardelli J. A., Clayton G. C., Mathis J. S., 1988, *ApJ*, **329**, L33
- Cardelli J. A., Clayton G. C., Mathis J. S., 1989, *ApJ*, **345**, 245
- Cepa J., et al., 2000, in Iye M., Moorwood A. F., eds, Society of Photo-Optical Instrumentation Engineers (SPIE) Conference Series Vol. 4008, Optical and IR Telescope Instrumentation and Detectors, pp 623–631, doi:[10.1117/12.395520](#)
- Chambers K. C., et al., 2016, arXiv e-prints, p. [arXiv:1612.05560](#)
- Chatzopoulos E., Wheeler J. C., Vinko J., 2012, *ApJ*, **746**, 121
- Chatzopoulos E., Wheeler J. C., Vinko J., Horvath Z. L., Nagy A., 2013, *ApJ*, **773**, 76
- Chen T.-W., et al., 2013, *ApJ*, **763**, L28
- Chen T. W., et al., 2015, *MNRAS*, **452**, 1567
- Chen K.-J., Woosley S. E., Sukhbold T., 2016, *ApJ*, **832**, 73
- Chen T.-W., Smartt S. J., Yates R. M., Nicholl M., Krühler T., Schady P., Dennefeld M., Inserra C., 2017a, *MNRAS*, **470**, 3566
- Chen T. W., et al., 2017b, *A&A*, **602**, A9
- Chevalier R. A., Fransson C., 2003, Supernova Interaction with a Circumstellar Medium, Springer Berlin Heidelberg, Berlin, Heidelberg, pp 171–194, doi:[10.1007/3-540-45863-8_10](#), https://doi.org/10.1007/3-540-45863-8_10
- Chevalier R. A., Irwin C. M., 2011, *ApJ*, **729**, L6
- Chonis T. S., Gaskell C. M., 2008, *AJ*, **135**, 264
- Chugai N. N., 2021, *MNRAS*, **508**, 6023
- Conley A., et al., 2006, *AJ*, **132**, 1707
- Cushing M. C., Vacca W. D., Rayner J. T., 2004, *PASP*, **116**, 362
- De Cia A., et al., 2018, *ApJ*, **860**, 100
- Denicoló G., Terlevich R., Terlevich E., 2002, *MNRAS*, **330**, 69
- Dessart L., 2019, *A&A*, **621**, A141
- Dessart L., Hillier D. J., Waldman R., Livne E., Blondin S., 2012, *MNRAS*, **426**, L76
- Dessart L., Hillier D. J., Woosley S., Livne E., Waldman R., Yoon S.-C., Langer N., 2015, *MNRAS*, **453**, 2189
- Elias-Rosa N., et al., 2006, *MNRAS*, **369**, 1880
- Fiore A., et al., 2021, *MNRAS*, **502**, 2120
- Gal-Yam A., 2012, *Science*, **337**, 927
- Gal-Yam A., 2019a, *ARA&A*, **57**, 305
- Gal-Yam A., 2019b, *ApJ*, **882**, 102
- Gal-Yam A., Yaron O., Pastorello A., Taubenberger S., Fraser M., Perley D., 2021, Transient Name Server AstroNote, [76](#), 1
- Gehrels N., et al., 2004, *ApJ*, **611**, 1005
- Ginzburg S., Balberg S., 2012, *ApJ*, **757**, 178
- Gomez S., Berger E., Hosseinzadeh G., Blanchard P. K., Nicholl M., Villar V. A., 2021, *ApJ*, **913**, 143
- Groves B., Brinchmann J., Walcher C. J., 2012, *MNRAS*, **419**, 1402
- Guillochon J., Nicholl M., Villar V. A., Mockler B., Narayan G., Mandel K. S., Berger E., Williams P. K. G., 2017, MOSFiT: Modular Open-Source Fitter for Transients (ascl:1710.006)
- Guillochon J., Nicholl M., Villar V. A., Mockler B., Narayan G., Mandel K. S., Berger E., Williams P. K. G., 2018, *ApJS*, **236**, 6
- (HEASARC) N. H. E. A. S. A. R. C., 2014, HEAsoft: Unified Release of FTOOLS and XANADU (ascl:1408.004)
- Harris J., Zaritsky D., 2009, *AJ*, **138**, 1243
- Harutyunyan A. H., et al., 2008, *A&A*, **488**, 383
- Heger A., Woosley S. E., 2002, *ApJ*, **567**, 532
- Holmbo S., et al., 2019, The Astronomer's Telegram, [12661](#), 1
- Hosseinzadeh G., Berger E., Metzger B. D., Gomez S., Nicholl M., Blanchard P., 2021, arXiv e-prints, p. [arXiv:2109.09743](#)
- Howell D. A., 2017, Superluminous Supernovae, Springer International Publishing, Cham, pp 431–458, doi:[10.1007/978-3-319-21846-5_41](#), https://doi.org/10.1007/978-3-319-21846-5_41
- Inserra C., 2019, *Nature Astronomy*, **3**, 697
- Inserra C., et al., 2013, *ApJ*, **770**, 128
- Inserra C., et al., 2017, *MNRAS*, **468**, 4642
- Jeffery D. J., Branch D., 1990, in Wheeler J. C., Piran T., Weinberg S., eds, Jerusalem Winter School for Theoretical Physics Vol. 6, Supernovae, p. 149
- Jerkstrand A., 2017, Spectra of Supernovae in the Nebular Phase, Springer International Publishing, Cham, pp 795–842, doi:[10.1007/978-3-319-21846-5_29](#), https://doi.org/10.1007/978-3-319-21846-5_29
- Jerkstrand A., et al., 2017, *ApJ*, **835**, 13
- Kangas T., et al., 2017, *MNRAS*, **469**, 1246
- Kaplan N., Soker N., 2020, *MNRAS*, **492**, 3013
- Kasen D., Bildsten L., 2010, *ApJ*, **717**, 245
- Kasen D., Woosley S. E., Heger A., 2011, *ApJ*, **734**, 102
- Kennicutt Robert C. J., 1998, *ARA&A*, **36**, 189
- Kewley L. J., Dopita M. A., 2002, *ApJS*, **142**, 35
- Kewley L. J., Ellison S. L., 2008, *ApJ*, **681**, 1183
- Khetan N., et al., 2021, *A&A*, **647**, A72
- Könyves-Tóth R., Vinkó J., 2020, arXiv e-prints, p. [arXiv:2011.00883](#)
- Lee C.-H., 2019, *ApJ*, **875**, 121
- Leloudas G., et al., 2012, *A&A*, **541**, A129
- Leloudas G., et al., 2015, *MNRAS*, **449**, 917
- Lin W. L., et al., 2020a, *MNRAS*, **497**, 318
- Lin W. L., Wang X. F., Wang L. J., Dai Z. G., 2020b, *ApJ*, **903**, L24
- Lunnan R., et al., 2014, *ApJ*, **787**, 138
- Lunnan R., et al., 2018a, *Nature Astronomy*, **2**, 887
- Lunnan R., et al., 2018b, *ApJ*, **852**, 81
- Lunnan R., et al., 2020, *ApJ*, **901**, 61
- Maiolino R., et al., 2008, *A&A*, **488**, 463
- Margalit B., Metzger B. D., Thompson T. A., Nicholl M., Sukhbold T., 2018, *MNRAS*, **475**, 2659
- Marino R. A., et al., 2013, *A&A*, **559**, A114
- Mattila S., et al., 2016, The Astronomer's Telegram, [8992](#), 1
- Mazzali P. A., Sullivan M., Pian E., Greiner J., Kann D. A., 2016, *MNRAS*, **458**, 3455
- McGaugh S. S., 1991, *ApJ*, **380**, 140
- Metzger B. D., Vurm I., Hascoët R., Beloborodov A. M., 2014, *MNRAS*, **437**, 703
- Minkowski R., 1941, *PASP*, **53**, 224
- Modjaz M., Gutierrez C. P., Arcavi I., 2019, *Nature Astronomy*, **3**, 717
- Moriya T. J., Tominaga N., 2012, *ApJ*, **747**, 118
- Moriya T. J., Sorokina E. I., Chevalier R. A., 2018, *Space Sci. Rev.*, **214**, 59
- Müller T., Prieto J. L., Pejcha O., Clocchiatti A., 2017, *ApJ*, **841**, 127
- Nadyozhin D. K., 1994, *ApJS*, **92**, 527
- Nicholl M., et al., 2014, *MNRAS*, **444**, 2096
- Nicholl M., et al., 2015a, *MNRAS*, **452**, 3869
- Nicholl M., et al., 2015b, *ApJ*, **807**, L18
- Nicholl M., et al., 2016, *ApJ*, **826**, 39
- Nicholl M., Berger E., Margutti R., Blanchard P. K., Milisavljevic D., Challis P., Metzger B. D., Chornock R., 2017a, *ApJ*, **835**, L8
- Nicholl M., Guillochon J., Berger E., 2017b, *ApJ*, **850**, 55
- Nicholl M., Berger E., Blanchard P. K., Gomez S., Chornock R., 2019, *ApJ*, **871**, 102
- Nicholl M., et al., 2020, *Nature Astronomy*, **4**, 893
- Ofek E. O., et al., 2014, *ApJ*, **781**, 42
- Pagel B. E. J., Edmunds M. G., Blackwell D. E., Chun M. S., Smith G., 1979, *MNRAS*, **189**, 95
- Parrag E., et al., 2021, *MNRAS*, **506**, 4819
- Pastorello A., et al., 2010, *ApJ*, **724**, L16
- Pastorello A., et al., 2021, Transient Name Server Classification Report, [2021-511](#), 1
- Perley D. A., et al., 2015, *ApJ*, **801**, 102
- Pignata G., et al., 2004, *MNRAS*, **355**, 178
- Planck Collaboration et al., 2016, *A&A*, **594**, A13
- Prentice S. J., et al., 2019, *MNRAS*, **485**, 1559
- Quimby R. M., et al., 2011, *Nature*, **474**, 487
- Rayner J. T., Toomey D. W., Onaka P. M., Denault A. J., Stahlberger W. E., Vacca W. D., Cushing M. C., Wang S., 2003, *PASP*, **115**, 362
- Renzou M., Farmer R., Justham S., Götberg Y., de Mink S. E., Zapartas E., Marchant P., Smith N., 2020, *A&A*, **640**, A56

- Richardson D., Jenkins Robert L. I., Wright J., Maddox L., 2014, *AJ*, **147**, 118
- Riess A. G., et al., 1999, *AJ*, **118**, 2675
- Riess A. G., Casertano S., Yuan W., Bowers J. B., Macri L., Zinn J. C., Scolnic D., 2021, *ApJ*, **908**, L6
- Roy R., et al., 2016, *A&A*, **596**, A67
- Schlafly E. F., Finkbeiner D. P., 2011, *The Astrophysical Journal*
- Schulze S., et al., 2018, *MNRAS*, **473**, 1258
- Skrutskie M. F., et al., 2006, *AJ*, **131**, 1163
- Smartt S. J., 2009, *Annual Review of Astronomy and Astrophysics*, **47**, 63
- Smartt S. J., et al., 2015, *A&A*, **579**, A40
- Smith N., 2017, *Interacting Supernovae: Types IIn and Ibn*. Springer International Publishing, Cham, pp 403–429, doi:10.1007/978-3-319-21846-5_38, https://doi.org/10.1007/978-3-319-21846-5_38
- Smith N., McCray R., 2007, *ApJ*, **671**, L17
- Smith N., et al., 2007, *ApJ*, **666**, 1116
- Smith N., et al., 2015, *MNRAS*, **449**, 1876
- Smith M., et al., 2016, *ApJ*, **818**, L8
- Soderberg A. M., et al., 2008, *Nature*, **453**, 469
- Soker N., Gilkis A., 2017, *ApJ*, **851**, 95
- Steavance H. F., Eldridge J. J., 2021, *MNRAS*, **504**, L51
- Stritzinger M., et al., 2002, *AJ*, **124**, 2100
- Tonry J. L., et al., 2012, *ApJ*, **750**, 99
- Tonry J. L., et al., 2018a, *ApJ*, **867**, 105
- Tonry J., et al., 2018b, Transient Name Server Discovery Report, **2018-1680**, 1
- Villar V. A., Nicholl M., Berger E., 2018, *ApJ*, **869**, 166
- Vurm I., Metzger B. D., 2021, *ApJ*, **917**, 77
- Wang S. Q., Wang L. J., Dai Z. G., Wu X. F., 2015, *ApJ*, **799**, 107
- Weiler K., 2003, *Supernovae and Gamma-Ray Bursters. Lecture Notes in Physics* Vol. 598, Springer, Berlin, Heidelberg, doi:10.1007/3-540-45863-8
- Woosley S. E., 2010, *ApJ*, **719**, L204
- Woosley S. E., 2017, *ApJ*, **836**, 244
- Woosley S. E., Blinnikov S., Heger A., 2007, *Nature*, **450**, 390
- Yan L., et al., 2015, *ApJ*, **814**, 108
- Yan L., et al., 2017a, *ApJ*, **840**, 57
- Yan L., et al., 2017b, *ApJ*, **848**, 6
- Yang Y., et al., 2020, *ApJ*, **902**, 46
- Yaron O., Gal-Yam A., 2012, *PASP*, **124**, 668
- Zaritsky D., Kennicutt Robert C. J., Huchra J. P., 1994, *ApJ*, **420**, 87
- Zou Y.-C., Cheng K. S., 2018, *Publ. Astron. Soc. Australia*, **35**, 32
- van Dokkum P. G., 2001, *PASP*, **113**, 1420

APPENDIX A: TABLES

This paper has been typeset from a $\text{\TeX}/\text{\LaTeX}$ file prepared by the author.

Table A1. $uvw1$, $uvm2$, $uvw2$ -filters observed (non K -corrected) aperture magnitudes (in AB system). Errors are in parentheses.

MJD	r. f. phase [days]	$uvw2$	$uvm2$	$uvw1$	instrument
58430.65	-31.89	20.17(0.12)	19.76(0.14)	18.90(0.09)	<i>Swift</i> /UVOT
58431.56	-31.03	20.21(0.12)	19.73(0.12)	18.65(0.08)	<i>Swift</i> /UVOT
58434.92	-27.87	19.92(0.11)	19.54(0.12)	18.47(0.08)	<i>Swift</i> /UVOT
58436.44	-26.44	19.88(0.11)	19.37(0.11)	18.39(0.08)	<i>Swift</i> /UVOT
58440.36	-22.74	19.88(0.17)	19.58(0.19)	18.16(0.11)	<i>Swift</i> /UVOT
58442.82	-20.43	19.65(0.10)	19.19(0.10)	18.20(0.08)	<i>Swift</i> /UVOT
58446.70	-16.77	19.70(0.10)	19.42(0.11)	18.24(0.07)	<i>Swift</i> /UVOT
58448.62	-14.96	19.56(0.10)	19.38(0.11)	18.34(0.08)	<i>Swift</i> /UVOT
58450.55	-13.14	19.71(0.10)	19.32(0.10)	18.27(0.07)	<i>Swift</i> /UVOT
58453.25	-10.60	19.80(0.10)	19.57(0.13)	18.25(0.07)	<i>Swift</i> /UVOT
58454.31	-9.60	19.92(0.11)	19.43(0.12)	18.22(0.07)	<i>Swift</i> /UVOT
58456.57	-7.47	19.77(0.10)	19.55(0.12)	18.28(0.07)	<i>Swift</i> /UVOT
58459.81	-4.42	20.00(0.11)	19.57(0.09)	18.36(0.07)	<i>Swift</i> /UVOT
58460.14	-4.11	19.88(0.11)	19.66(0.10)	18.22(0.07)	<i>Swift</i> /UVOT
58465.49	0.93	19.95(0.11)	19.83(0.11)	18.45(0.07)	<i>Swift</i> /UVOT
58467.51	2.84	20.03(0.12)	19.95(0.11)	18.45(0.08)	<i>Swift</i> /UVOT
58474.21	9.15	20.13(0.12)	20.10(0.11)	18.71(0.08)	<i>Swift</i> /UVOT
58476.78	11.57	20.64(0.18)	20.25(0.18)	18.80(0.10)	<i>Swift</i> /UVOT
58482.62	17.07	20.50(0.16)	20.44(0.18)	19.08(0.11)	<i>Swift</i> /UVOT
58485.38	19.67	20.48(0.16)	20.60(0.16)	19.03(0.10)	<i>Swift</i> /UVOT
58491.86	25.78	20.85(0.16)	20.83(0.14)	19.18(0.09)	<i>Swift</i> /UVOT
58496.65	30.29	21.04(0.17)	21.10(0.21)	19.53(0.11)	<i>Swift</i> /UVOT
58504.78	37.95	21.30(0.36)	21.76(0.47)	19.85(0.22)	<i>Swift</i> /UVOT
58508.66	41.61	21.57(0.21)	21.74(0.22)	19.85(0.12)	<i>Swift</i> /UVOT
58512.47	45.20	21.42(0.20)	21.97(0.26)	20.45(0.17)	<i>Swift</i> /UVOT
58516.32	48.82	21.70(0.24)	22.54(0.37)	20.31(0.16)	<i>Swift</i> /UVOT
58559.71	89.70	23.34(0.89)	23.29(0.67)	21.40(0.34)	<i>Swift</i> /UVOT
58569.81	99.22	22.54(0.64)	24.75(3.28)	21.63(0.58)	<i>Swift</i> /UVOT

Table A2. u , g , r , i , z -filter observed (non K -corrected, non S-corrected) magnitudes (in AB system). Errors are in parentheses.

MJD	r. f. phase [days]	u	g	r	i	z	instrument
58413.54	-48.01	-	-	19.31(0.16)	-	-	ATLAS
58423.53	-38.60	-	-	18.54(0.19)	-	-	ATLAS
58424.54	-37.65	-	-	18.51(0.14)	-	-	ATLAS
58426.12	-36.16	-	18.05(0.01)	17.90(0.01)	17.76(0.02)	-	LCO+Sinistro
58427.17	-35.18	-	-	17.91(0.01)	17.86(0.01)	-	LCO+Sinistro
58428.33	-34.08	-	17.87(0.01)	17.73(0.01)	17.70(0.01)	-	LCO+Sinistro
58428.52	-33.90	-	-	17.85(0.03)	-	-	ATLAS
58431.14	-31.43	-	17.49(0.01)	17.43(0.01)	17.34(0.01)	-	LCO+Sinistro
58432.52	-30.13	-	-	17.41(0.04)	-	-	ATLAS
58433.03	-29.65	-	17.28(0.01)	17.21(0.01)	17.12(0.01)	-	LCO+Sinistro
58433.59	-29.12	-	-	17.30(0.12)	-	-	ATLAS
58433.94	-28.80	-	17.23(0.01)	17.11(0.01)	17.07(0.01)	-	LCO+Sinistro
58435.02	-27.77	-	-	-	17.05(0.02)	-	LCO+Sinistro
58436.15	-26.71	-	17.08(0.01)	17.02(0.01)	16.95(0.01)	-	LCO+Sinistro
58436.49	-26.39	-	-	16.97(0.04)	-	-	ATLAS
58436.85	-26.05	-	17.16(0.01)	16.94(0.01)	16.86(0.01)	-	LCO+Sinistro
58437.00	-25.91	18.19(0.03)	16.97(0.02)	16.86(0.01)	16.82(0.01)	16.97(0.01)	NOT+ALFOSC
58437.12	-25.80	-	17.10(0.01)	16.93(0.01)	16.89(0.01)	-	LCO+Sinistro
58437.51	-25.43	-	-	16.92(0.03)	-	-	ATLAS
58438.49	-24.51	-	17.15(0.01)	16.95(0.02)	16.80(0.01)	-	LCO+Sinistro
58440.24	-22.86	-	16.92(0.01)	16.75(0.01)	16.71(0.01)	-	LCO+Sinistro
58441.27	-21.89	-	16.61(0.03)	16.70(0.03)	16.66(0.02)	-	LCO+Sinistro
58441.30	-21.86	-	16.88(0.01)	16.71(0.01)	16.66(0.01)	-	LCO+Sinistro
58442.44	-20.78	-	-	16.69(0.05)	-	-	ATLAS
58443.20	-20.07	-	16.83(0.01)	16.68(0.01)	16.57(0.01)	-	LCO+Sinistro
58448.47	-15.10	-	-	16.52(0.03)	-	-	ATLAS
58449.23	-14.39	-	16.82(0.01)	-	16.55(0.01)	-	LCO+Sinistro
58449.25	-14.37	-	16.48(0.02)	16.48(0.01)	16.34(0.01)	-	LCO+Sinistro
58449.46	-14.17	-	-	16.57(0.01)	-	-	ATLAS
58450.47	-13.22	-	-	16.49(0.04)	-	-	ATLAS
58451.47	-12.28	-	-	16.41(0.02)	-	-	ATLAS
58452.10	-11.68	-	16.31(0.02)	16.47(0.02)	16.33(0.02)	-	LCO+Sinistro
58453.00	-10.84	17.71(0.03)	16.43(0.02)	16.33(0.01)	16.40(0.01)	16.42(0.01)	NOT+ALFOSC
58453.44	-10.42	-	-	16.42(0.03)	-	-	ATLAS
58453.58	-10.29	-	16.59(0.0)	16.39(0.01)	16.34(0.01)	-	LCO+Sinistro
58454.12	-9.78	-	16.43(0.01)	16.40(0.01)	16.34(0.01)	-	LCO+Sinistro
58456.09	-7.93	-	-	16.43(0.01)	-	-	LCO+Sinistro
58456.48	-7.56	-	16.69(0.01)	16.39(0.01)	16.33(0.01)	-	LCO+Sinistro
58456.86	-7.20	-	16.40(0.03)	16.40(0.02)	16.34(0.02)	-	Schmidt
58460.22	-4.04	-	16.51(0.01)	16.43(0.01)	16.39(0.01)	-	LCO+Sinistro
58460.23	-4.02	-	16.66(0.03)	16.39(0.02)	16.28(0.04)	-	LCO+Sinistro
58460.41	-3.85	-	-	16.45(0.02)	-	-	ATLAS
58461.93	-2.43	-	16.58(0.01)	16.33(0.01)	-	-	LCO+Sinistro
58462.09	-2.28	-	-	16.34(0.01)	16.28(0.01)	-	LCO+Sinistro
58462.09	-2.27	-	-	-	16.28(0.01)	-	LCO+Sinistro
58463.17	-1.26	-	16.61(0.01)	16.38(0.01)	16.26(0.01)	-	LCO+Sinistro
58463.84	-0.63	-	16.61(0.01)	16.41(0.02)	16.38(0.02)	-	LCO+Sinistro
58465.49	0.93	-	-	16.36(0.01)	-	-	ATLAS
58467.87	3.18	-	16.72(0.01)	16.43(0.01)	16.28(0.01)	-	LCO+Sinistro
58471.39	6.49	-	-	16.43(0.01)	-	-	ATLAS
58474.32	9.25	-	16.75(0.03)	-	16.34(0.04)	-	LCO+Sinistro
58476.55	11.35	-	16.82(0.01)	16.53(0.01)	16.32(0.01)	-	LCO+Sinistro
58478.52	13.21	-	16.85(0.01)	16.57(0.01)	16.33(0.01)	-	LCO+Sinistro
58479.38	14.02	-	-	16.44(0.02)	-	-	ATLAS
58480.86	15.41	17.68(0.01)	16.57(0.01)	-	16.37(0.01)	16.36(0.04)	1.82m+AFOSC
58481.45	15.96	-	16.67(0.0)	16.47(0.01)	16.34(0.01)	-	LCO+Sinistro
58481.56	16.07	-	16.94(0.02)	16.58(0.01)	16.35(0.01)	-	LCO+Sinistro
58485.36	19.65	-	-	16.64(0.03)	-	-	ATLAS
58486.86	21.07	-	16.89(0.02)	16.66(0.02)	16.42(0.02)	-	LCO+Sinistro
58488.17	22.30	-	16.79(0.01)	16.51(0.01)	16.35(0.01)	-	LCO+Sinistro

Table A2. (continued).

MJD	r. f. phase [days]	<i>u</i>	<i>g</i>	<i>r</i>	<i>i</i>	<i>z</i>	instrument
58489.35	23.41	-	-	16.58(0.03)	-	-	ATLAS
58489.92	23.95	17.85(0.01)	16.71(0.01)	-)	16.41(0.01)	16.38(0.03)	1.82m+AFOSC
58490.82	24.79	-	16.66(0.01)	16.62(0.01)	16.43(0.01)	-	LCO+Sinistro
58492.36	26.25	-	-	16.55(0.03)	-	-	ATLAS
58493.07	26.91	-	16.83(0.01)	16.54(0.01)	16.39(0.01)	-	LCO+Sinistro
58495.35	29.07	-	-	16.54(0.01)	-	-	ATLAS
58496.81	30.44	-	16.99(0.02)	16.80(0.03)	16.57(0.04)	-	LCO+Sinistro
58496.87	30.50	18.40(0.01)	16.75(0.02)	16.57(0.01)	16.43(0.01)	16.38(0.01)	NOT+ALFOSC
58497.34	30.94	-	-	16.85(0.07)	-	-	ATLAS
58498.06	31.62	-	16.86(0.01)	16.61(0.01)	16.43(0.01)	-	LCO+Sinistro
58501.33	34.70	-	-	16.62(0.03)	-	-	ATLAS
58502.35	35.66	-	-	16.71(0.02)	-	-	ATLAS
58502.82	36.10	-	17.12(0.02)	-	16.55(0.02)	-	LCO+Sinistro
58503.37	36.62	-	-	16.80(0.05)	-	-	ATLAS
58504.38	37.57	-	-	16.66(0.06)	-	-	ATLAS
58505.06	38.21	-	16.90(0.02)	16.69(0.02)	16.48(0.02)	-	LCO+Sinistro
58505.25	38.39	-	-	16.69(0.10)	-	-	ATLAS
58505.87	38.98	18.63(0.01)	16.94(0.02)	16.59(0.02)	16.54(0.01)	16.40(0.01)	NOT+ALFOSC
58507.32	40.34	-	-	16.69(0.02)	-	-	ATLAS
58508.08	41.05	-	17.10(0.01)	16.72(0.01)	16.54(0.01)	-	LCO+Sinistro
58508.11	41.09	-	17.04(0.02)	16.78(0.05)	16.60(0.01)	-	LCO+Sinistro
58509.31	42.22	-	-	17.01(0.05)	-	-	ATLAS
58510.32	43.17	-	-	16.82(0.06)	-	-	ATLAS
58513.31	45.99	-	-	16.94(0.13)	-	-	ATLAS
58516.32	48.82	-	-	16.92(0.03)	-	-	ATLAS
58518.04	50.44	-	17.43(0.01)	16.93(0.01)	16.77(0.01)	-	LCO+Sinistro
58519.88	52.17	19.10(0.05)	17.26(0.01)	16.91(0.01)	16.74(0.01)	16.56(0.01)	NOT+ALFOSC
58521.04	53.26	-	17.46(0.01)	16.99(0.01)	16.80(0.01)	-	LCO+Sinistro
58523.06	55.17	-	17.47(0.01)	17.02(0.01)	16.82(0.01)	-	LCO+Sinistro
58526.00	57.94	-	-	17.18(0.01)	16.93(0.01)	-	Post Observatory
58529.29	61.04	-	-	17.15(0.04)	-	-	ATLAS
58531.15	62.79	-	17.66(0.02)	17.19(0.02)	17.04(0.02)	-	LCO+Sinistro
58532.24	63.82	-	-	17.22(0.08)	-	-	ATLAS
58534.86	66.29	19.87(0.02)	17.68(0.02)	17.30(0.01)	17.12(0.01)	16.94(0.02)	NOT+ALFOSC
58537.24	68.53	-	-	17.41(0.05)	-	-	ATLAS
58538.14	69.38	-	17.91(0.01)	17.31(0.01)	17.14(0.02)	-	LCO+Sinistro
58541.22	72.28	-	-	17.53(0.01)	-	-	ATLAS
58542.78	73.75	19.81(0.05)	18.02(0.03)	17.55(0.03)	17.14(0.04)	17.07(0.10)	1.82m+AFOSC
58543.80	74.72	19.90(0.17)	17.81(0.06)	17.43(0.05)	17.27(0.05)	-	Schmidt
58545.09	75.92	-	18.08(0.01)	17.58(0.01)	17.32(0.01)	-	LCO+Sinistro
58545.23	76.06	-	-	17.55(0.04)	-	-	ATLAS
58552.24	82.66	-	-	17.96(0.11)	-	-	ATLAS
58557.26	87.39	-	-	17.84(0.06)	-	-	ATLAS
58560.27	90.23	-	-	17.96(0.26)	-	-	ATLAS
58561.23	91.13	-	-	17.98(0.18)	-	-	ATLAS
58565.27	94.94	-	-	18.04(0.17)	-	-	ATLAS
58569.25	98.69	-	-	18.14(0.01)	-	-	ATLAS
58573.25	102.46	-	-	18.47(0.01)	-	-	ATLAS
58719.54	240.29	-	-	20.57(0.46)	-	-	ATLAS
58731.51	251.56	-	-	19.89(0.31)	-	-	1.2m+KeplerCam
58731.51	251.56	-	-	-	-	-	1.2m+KeplerCam
58741.15	260.64	-	21.21(0.07)	20.66(0.03)	20.49(0.02)	-	NOT+ALFOSC
58751.13	270.05	-	-	20.54(0.05)	-	-	OSIRIS
58752.55	271.39	-	-	20.72(0.34)	-	-	ATLAS
58756.52	275.13	-	-	20.95(0.31)	-	-	ATLAS
58834.37	348.47	-	-	21.63(0.14)	-	-	1.2m+KeplerCam
58838.38	352.25	-	-	≥20.93	-	-	1.2m+KeplerCam
58844.36	357.89	-	-	21.82(0.19)	-	-	ATLAS
58861.29	373.84	-	-	21.20(0.08)	≥21.08(0.01)	-	1.2m+KeplerCam
58862.27	374.76	-	-	21.28(0.17)	-	-	1.2m+KeplerCam
58867.25	379.45	-	22.73(0.23)	21.58(0.07)	-	-	1.2m+KeplerCam

Table A2. (continued.)

MJD	r. f. phase [days]	<i>u</i>	<i>g</i>	<i>r</i>	<i>i</i>	<i>z</i>	instrument
58872.28	384.19	-	22.62(0.18)	-	-	-	1.2m+KeplerCam
58872.29	384.20	-	-	21.22(0.07)	21.51(0.07)	-	1.2m+KeplerCam
58873.28	385.13	-	-	21.84(0.11)	-	-	1.2m+KeplerCam
58873.29	385.14	-	-	21.39(0.10)	-	-	1.2m+KeplerCam
58904.87	414.90	-	$\geq 22.63(0.11)$	$\geq 21.74(0.07)$	-	$\geq 21.68(0.20)$	NOT+ALFOSC

Table A3. U , B , V -observed (non K -corrected, non S-corrected) magnitudes (in AB system).

MJD	r. f. phase [days]	U	B	V	instrument
58426.12	-36.16	-	18.37(0.01)	17.90(0.02)	LCO+Sinistro
58427.15	-35.19	-	18.09(0.02)	17.87(0.01)	LCO+Sinistro
58428.31	-34.1	-	17.95(0.02)	17.69(0.01)	LCO+Sinistro
58429.29	-33.17	-	17.83(0.04)	17.56(0.01)	LCO+Sinistro
58430.66	-31.88	16.80(0.07)	17.76(0.08)	17.52(0.12)	<i>Swift</i> /UVOT
58431.11	-31.46	-	17.56(0.01)	17.37(0.01)	LCO+Sinistro
58431.56	-31.03	16.77(0.07)	17.76(0.07)	17.38(0.10)	<i>Swift</i> /UVOT
58432.11	-30.52	-	17.39(0.01)	17.27(0.01)	LCO+Sinistro
58433.92	-28.81	-	17.38(0.01)	17.06(0.01)	LCO+Sinistro
58434.92	-27.87	16.46(0.07)	17.57(0.07)	17.11(0.1)	<i>Swift</i> /UVOT
58435.0	-27.79	-	17.36(0.01)	-	LCO+Sinistro
58436.14	-26.72	-	17.18(0.02)	16.96(0.01)	LCO+Sinistro
58436.44	-26.44	16.41(0.06)	17.31(0.06)	17.12(0.09)	<i>Swift</i> /UVOT
58436.85	-26.05	-	17.73(0.03)	16.97(0.07)	LCO+Sinistro
58436.99	-25.92	-	17.16(0.02)	16.82(0.01)	NOT+ALFOSC
58437.1	-25.81	16.29(0.04)	17.1(0.02)	16.87(0.01)	LCO+Sinistro
58437.92	-25.04	-	17.17(0.02)	-	LCO+Sinistro
58438.01	-24.96	16.45(0.05)	-	16.87(0.01)	LCO+Sinistro
58438.01	-24.96	-	17.08(0.01)	-	LCO+Sinistro
58438.03	-24.94	16.19(0.01)	16.82(0.02)	16.83(0.04)	LCO+Sinistro
58438.49	-24.51	-	17.25(0.03)	17.14(0.09)	LCO+Sinistro
58440.21	-22.88	16.16(0.07)	-	16.77(0.03)	LCO+Sinistro
58440.36	-22.74	16.14(0.09)	17.15(0.09)	16.87(0.14)	<i>Swift</i> /UVOT
58441.27	-21.89	-	17.09(0.04)	16.64(0.02)	LCO+Sinistro
58441.28	-21.88	16.02(0.03)	16.93(0.02)	16.66(0.01)	LCO+Sinistro
58442.82	-20.43	16.11(0.06)	17.0(0.06)	16.61(0.08)	<i>Swift</i> /UVOT
58443.18	-20.09	16.14(0.03)	16.84(0.02)	16.53(0.02)	LCO+Sinistro
58446.7	-16.77	16.06(0.06)	17.02(0.06)	16.65(0.08)	<i>Swift</i> /UVOT
58448.62	-14.96	15.92(0.06)	16.93(0.06)	16.50(0.07)	<i>Swift</i> /UVOT
58449.22	-14.4	15.92(0.05)	16.75(0.04)	16.23(0.02)	LCO+Sinistro
58449.23	-14.39	-	16.8(0.03)	16.57(0.02)	LCO+Sinistro
58450.56	-13.13	16.00(0.06)	16.78(0.05)	16.52(0.07)	<i>Swift</i> /UVOT
58452.1	-11.68	-	16.64(0.08)	16.40(0.01)	LCO+Sinistro
58452.99	-10.84	-	16.66(0.01)	16.36(0.01)	NOT+ALFOSC
58453.25	-10.6	15.92(0.06)	16.75(0.05)	16.45(0.07)	<i>Swift</i> /UVOT
58453.56	-10.31	15.96(0.04)	16.71(0.01)	16.41(0.01)	LCO+Sinistro
58454.12	-9.78	-	16.63(0.03)	16.37(0.01)	LCO+Sinistro
58454.31	-9.6	15.85(0.06)	16.83(0.05)	16.38(0.07)	<i>Swift</i> /UVOT
58456.07	-7.94	15.88(0.01)	-	16.34(0.01)	LCO+Sinistro
58456.57	-7.47	15.94(0.06)	16.80(0.05)	16.38(0.07)	<i>Swift</i> /UVOT
58456.85	-7.21	-	16.5(0.02)	16.26(0.02)	AFOSC
58456.85	-7.21	-	-	16.41(0.01)	Schmidt
58459.81	-4.42	15.88(0.06)	16.77(0.06)	16.38(0.07)	<i>Swift</i> /UVOT
58460.14	-4.11	15.88(0.06)	16.79(0.06)	16.38(0.08)	<i>Swift</i> /UVOT
58460.19	-4.06	15.91(0.04)	16.57(0.01)	16.33(0.01)	LCO+Sinistro
58461.92	-2.43	15.91(0.03)	16.58(0.03)	16.36(0.02)	LCO+Sinistro
58462.07	-2.29	15.91(0.02)	16.56(0.01)	16.33(0.01)	LCO+Sinistro
58463.17	-1.25	-	16.64(0.01)	16.45(0.01)	LCO+Sinistro
58463.82	-0.64	15.92(0.03)	16.63(0.02)	16.36(0.01)	LCO+Sinistro
58465.49	0.93	15.94(0.06)	16.68(0.06)	16.34(0.07)	<i>Swift</i> /UVOT
58467.51	2.84	15.88(0.06)	16.83(0.06)	16.47(0.08)	<i>Swift</i> /UVOT
58467.88	3.18	-	17.18(0.07)	16.38(0.02)	LCO+Sinistro
58474.21	9.15	16.13(0.06)	16.94(0.06)	16.44(0.07)	<i>Swift</i> /UVOT
58474.3	9.23	-	-	16.41(0.07)	LCO+Sinistro
58476.78	11.57	16.20(0.07)	16.93(0.07)	16.49(0.10)	<i>Swift</i> /UVOT
58478.52	13.21	-	16.91(0.03)	16.61(0.03)	LCO+Sinistro
58479.3	13.94	-	16.72(0.03)	-	LCO+Sinistro
58480.85	15.4	-	16.75(0.02)	16.48(0.02)	AFOSC
58481.43	15.95	-	16.82(0.02)	16.43(0.01)	LCO+Sinistro
58481.56	16.07	-	16.90(0.06)	16.52(0.01)	LCO+Sinistro

Table A3. (continued.)

MJD	r. f. phase [days]	<i>U</i>	<i>B</i>	<i>V</i>	instrument
58482.62	17.07	16.20(0.07)	16.87(0.07)	16.57(0.09)	<i>Swift</i> /UVOT
58485.38	19.67	16.33(0.07)	16.92(0.07)	16.54(0.09)	<i>Swift</i> /UVOT
58486.86	21.07	-	17.02(0.05)	16.59(0.03)	LCO+Sinistro
58488.15	22.28	-	16.85(0.02)	16.51(0.01)	LCO+Sinistro
58489.92	23.95	-	16.86(0.03)	16.55(0.02)	AFOSC
58491.86	25.78	16.55(0.07)	17.09(0.06)	16.69(0.08)	<i>Swift</i> /UVOT
58493.06	26.91	-	16.87(0.02)	16.57(0.01)	LCO+Sinistro
58496.65	30.29	16.68(0.07)	17.24(0.07)	16.67(0.09)	<i>Swift</i> /UVOT
58496.81	30.44	-	17.11(0.02)	16.66(0.02)	LCO+Sinistro
58496.86	30.49	-	17.03(0.01)	16.60(0.01)	NOT+ALFOSC
58498.05	31.61	-	17.02(0.04)	16.67(0.02)	LCO+Sinistro
58502.81	36.09	-	17.15(0.03)	16.72(0.01)	LCO+Sinistro
58504.78	37.95	17.0(0.14)	17.35(0.12)	16.86(0.16)	<i>Swift</i> /UVOT
58505.87	38.98	-	17.25(0.01)	16.78(0.01)	NOT+ALFOSC
58508.07	41.05	-	17.23(0.01)	16.77(0.01)	LCO+Sinistro
58508.11	41.09	-	17.32(0.03)	16.97(0.07)	LCO+Sinistro
58508.66	41.61	17.19(0.08)	17.40(0.07)	16.73(0.08)	<i>Swift</i> /UVOT
58512.47	45.2	17.22(0.08)	17.50(0.07)	16.85(0.08)	<i>Swift</i> /UVOT
58516.32	48.82	17.34(0.09)	17.62(0.07)	16.83(0.08)	<i>Swift</i> /UVOT
58518.04	50.44	-	17.59(0.03)	17.04(0.02)	LCO+Sinistro
58519.86	52.16	-	17.57(0.01)	16.97(0.01)	NOT+ALFOSC
58521.03	53.26	-	17.66(0.02)	16.97(0.03)	LCO+Sinistro
58523.06	55.17	-	17.71(0.02)	17.14(0.01)	LCO+Sinistro
58526.57	58.48	-	18.01(0.06)	17.23(0.04)	Post Observatory
58528.76	60.54	-	17.80(0.13)	17.19(0.05)	Schmidt
58531.14	62.79	-	17.97(0.04)	17.32(0.03)	LCO+Sinistro
58531.61	63.23	-	18.04(0.04)	17.30(0.02)	Post Observatory
58534.85	66.28	-	18.14(0.02)	17.41(0.01)	NOT+ALFOSC
58538.12	69.36	-	18.19(0.02)	17.48(0.01)	LCO+Sinistro
58538.64	69.85	-	18.25(0.03)	17.49(0.02)	Post Observatory
58542.78	73.75	-	18.18(0.04)	17.68(0.03)	AFOSC
58543.8	74.71	-	18.31(0.08)	17.64(0.03)	Schmidt
58544.65	75.51	-	18.45(0.03)	17.62(0.02)	Post Observatory
58545.07	75.91	-	18.38(0.04)	17.69(0.05)	LCO+Sinistro
58559.72	89.71	18.97(0.26)	19.07(0.21)	17.86(0.17)	<i>Swift</i> /UVOT
58569.81	99.22	19.19(0.45)	19.03(0.29)	18.18(0.32)	<i>Swift</i> /UVOT
58741.14	260.64	-	-	21.05(0.03)	NOT+ALFOSC

Table A4. *J*, *H*, *K_s*-observed (non *K*-corrected) magnitudes (in AB system). Errors are in parentheses.

MJD	r. f. phase [days]	<i>J</i>	<i>H</i>	<i>K_s</i>	instrument
58512.96	45.56	15.60(0.01)	15.91(0.01)	16.75(0.01)	NOT+NOTCam
58546.87	77.51	16.21(0.02)	16.36(0.02)	17.37(0.03)	NOT+NOTCam
58563.85	93.50	-	17.77(0.04)	17.89(0.04)	NOT+NOTCam

Table A5. *W1*, *W2*-observed (non *K*-corrected) magnitudes (in AB system). Errors are in parentheses.

MJD	r. f. phase [days]	<i>W1</i>	<i>W2</i>	instrument
58507.39	40.04	17.95(0.07)	18.33(0.13)	WISE
58712.64	233.69	19.13(0.16)	≥ 18.61	WISE

Table A6. S-corrections for Schmidt and AFOSC filters (Asiago observatory).

MJD	<i>B</i>	<i>g</i>	<i>V</i>	<i>r</i>	<i>i</i>
58430.25	-0.02	0.01	0.018	0.113	0.053
58437.02	-0.019	0.014	0.022	0.122	0.048
58437.14	-0.017	0.014	0.019	0.127	0.06
58440.23	-0.027	0.012	0.018	0.101	0.064
58452.97	-0.014	0.018	0.022	0.122	0.05
58456.79	-0.004	0.019	0.021	0.115	-0.206
58460.21	-0.011	0.021	0.022	0.133	0.052
58468.16	-0.009	0.026	0.028	0.139	0.073
58480.81	-0.015	0.027	0.024	0.139	0.077
58489.87	-0.019	0.029	0.024	0.139	0.076
58491.12	-0.022	0.027	0.018	0.146	0.094
58496.89	-0.033	0.03	0.022	0.147	0.093
58505.86	-0.037	0.03	0.022	0.152	0.109
58519.89	-0.058	0.031	0.023	0.152	0.105
58522.04	-0.042	0.022	0.019	0.147	0.105
58534.87	-0.067	0.033	0.027	0.148	0.124
58542.81	-0.08	0.032	0.022	0.146	0.117
58543.80	-0.086	0.028	0.02	0.14	0.117
58751.14	-0.052	0.044	-0.013	0.124	-0.154

Table A7. S-corrections for Sinistro (LCO).

MJD	<i>B</i>	<i>g</i>	<i>V</i>	<i>r</i>	<i>i</i>
58430.25	-0.009	0.003	0.009	0.004	-0.005
58437.02	-0.008	0.004	0.003	0.007	-0.002
58437.14	-0.008	0.005	0.011	0.005	-0.001
58440.23	-0.009	0.004	0.009	-0.007	-0.0
58452.97	-0.005	0.008	-0.002	0.008	-0.002
58456.79	-0.005	0.012	-0.012	0.014	-0.101
58460.21	-0.004	0.011	-0.001	0.014	-0.007
58468.16	-0.002	0.015	-0.012	0.018	-0.004
58480.81	-0.001	0.015	-0.011	0.025	0.002
58489.87	-0.002	0.018	-0.015	0.029	-0.001
58491.12	-0.001	0.015	-0.004	0.034	-0.002
58496.89	-0.002	0.017	-0.014	0.044	0.002
58505.86	-0.003	0.016	-0.012	0.049	0.005
58519.89	-0.006	0.016	-0.018	0.058	0.005
58522.04	-0.006	0.01	-0.007	0.048	0.002
58534.87	-0.009	0.016	-0.024	0.054	0.005
58542.81	-0.01	0.016	-0.022	0.058	0.009
58543.80	-0.009	0.011	-0.018	0.052	0.01
58751.14	-0.015	0.033	-0.04	0.062	-0.013

Table A8. S-corrections for NOT filters.

MJD	<i>B</i>	<i>g</i>	<i>V</i>	<i>r</i>	<i>i</i>
58430.25	-0.013	0.001	0.008	0.011	-0.008
58437.02	-0.013	-0.004	0.005	0.013	-0.011
58437.14	-0.014	-0.002	0.011	0.015	-0.013
58440.23	-0.015	-0.005	0.007	0.002	0.011
58452.97	-0.01	-0.001	0.002	0.014	-0.01
58456.79	-0.008	0.007	-0.005	0.019	-0.313
58460.21	-0.008	0.001	0.004	0.022	-0.019
58468.16	-0.006	0.001	-0.004	0.022	0.011
58480.81	-0.008	-0.001	-0.003	0.026	0.031
58489.87	-0.012	-0.001	-0.005	0.028	0.033
58491.12	-0.009	-0.004	0.003	0.036	0.034
58496.89	-0.013	-0.009	-0.003	0.041	0.052
58505.86	-0.015	-0.011	-0.002	0.045	0.07
58519.89	-0.023	-0.018	-0.005	0.047	0.068
58522.04	-0.019	-0.012	0.001	0.041	0.065
58534.87	-0.027	-0.023	-0.007	0.043	0.089
58542.81	-0.031	-0.026	-0.007	0.05	0.09
58543.80	-0.034	-0.028	-0.004	0.047	0.086
58751.14	-0.021	0.003	-0.025	0.068	-0.251

Table A9. S-corrections for *Swift*/UVOT.

MJD	<i>B</i>	<i>V</i>
58430.25	-0.017	0.009
58437.02	-0.018	0.008
58437.14	-0.017	0.019
58440.23	-0.02	0.006
58452.97	-0.014	0.011
58456.79	-0.014	0.005
58460.21	-0.01	0.019
58468.16	-0.008	0.012
58480.81	-0.007	0.016
58489.87	-0.005	0.02
58491.12	-0.005	0.034
58496.89	-0.009	0.029
58505.86	-0.011	0.034
58519.89	-0.018	0.033
58522.04	-0.014	0.034
58534.87	-0.025	0.033
58542.81	-0.026	0.031
58543.80	-0.025	0.035
58751.14	-0.024	0.049

Table A10. Estimated uncertainties ΔS_{corr} for the filters u, U, z, J, H, K_s (for each instrument) divided in two temperature ranges (see text).

	5000 K < T < 10000 K	10000 K < T < 20000 K
NOT+ALFOSC/NOTCam	$\Delta S_{\text{corr},u} = 0.30$	$\Delta S_{\text{corr},u} = 0.20$
	$\Delta S_{\text{corr},z} = 0.03$	$\Delta S_{\text{corr},z} = 0.01$
	$\Delta S_{\text{corr},J} = 0.1$	$\Delta S_{\text{corr},J} = 0.1$
	$\Delta S_{\text{corr},H} = 0.1$	$\Delta S_{\text{corr},H} = 0.1$
	$\Delta S_{\text{corr},K_s} = 0.1$	$\Delta S_{\text{corr},K_s} = 0.1$
Schmidt/AFOSC	$\Delta S_{\text{corr},u} = 0.3$	$\Delta S_{\text{corr},u} = 0.2$
	$\Delta S_{\text{corr},z} = 0.3$	$\Delta S_{\text{corr},z} = -0.001$
LCO+Sinistro	$\Delta S_{\text{corr},z} = 0.001 \text{ mag}$	$\Delta S_{\text{corr},z} = 0.005 \text{ mag}$
<i>Swift</i> /UVOT	$\Delta S_{\text{corr},U} = 0.2 \text{ mag}$	$\Delta S_{\text{corr},U} = 0.05 \text{ mag}$

Table A11. K -corrections expressed in magnitudes.

rest-frame phase [days]	$uvw2$ filter	$uvm2$ filter	$uvw1$ filter	u filter	U filter	B filter	g filter	V filter	r filter	i filter	z filter	J filter	H filter	K_s filter
-32.36	-0.106	-0.098	0.031	0.191	0.191	0.009	-0.008	0.030	-0.002	0.043	-0.206	-0.154	-0.030	0.402
-25.98	-0.100	-0.103	0.037	0.166	0.173	-0.015	-0.022	0.028	0.004	0.068	-0.203	-0.159	-0.030	0.148
-25.87	-0.102	-0.105	0.037	0.165	0.173	-0.011	-0.016	0.038	0.005	0.131	-0.203	-0.159	-0.030	0.146
-22.96	-0.083	-0.055	0.080	0.129	0.137	-0.020	-0.023	0.028	0.013	-0.012	-0.202	-0.147	-0.033	0.089
-10.96	-0.064	-0.052	0.122	0.150	0.155	-0.013	-0.025	0.014	0.003	0.071	-0.214	-0.129	-0.032	-0.022
-7.36	-0.085	-0.060	0.146	0.127	0.135	0.020	-0.028	-	-	-	-0.191	-0.142	-0.038	-0.011
-4.15	-0.040	0.022	0.148	0.136	0.152	-0.004	-0.020	0.021	0.008	0.097	-0.195	-0.129	-0.039	-0.010
3.35	-0.030	0.038	0.194	0.129	0.131	-0.017	-0.037	-0.019	-0.052	0.034	-0.200	-0.127	-0.038	-0.017
15.27	-0.046	-0.002	0.276	0.080	0.084	-0.03	-0.043	-0.005	-0.023	0.006	-0.171	-0.139	-0.046	0.003
23.81	-0.042	0.080	0.281	0.083	0.100	-0.045	-0.058	-0.032	-0.049	-0.010	-0.164	-0.132	-0.051	0.018
24.99	-0.048	0.081	0.272	0.106	0.129	-0.05	-0.062	-0.001	-0.007	0.000	-0.168	-0.133	-0.050	0.015
30.42	-0.057	0.082	0.251	0.181	0.215	-0.076	-0.088	-0.032	-0.066	-0.058	-0.16	-0.122	-0.054	0.031
38.87	-0.067	0.097	0.288	0.178	0.218	-0.086	-0.096	-0.035	-0.054	-0.091	-0.138	-0.116	-0.067	0.076
52.09	-0.079	0.140	0.285	0.209	0.255	-0.126	-0.127	-0.051	-0.056	-0.068	-0.144	-0.100	-0.075	0.167
54.13	-0.094	0.121	0.274	0.228	0.277	-0.111	-0.114	-0.052	-0.063	-0.089	-0.147	-0.100	-0.073	0.179
66.21	-0.182	0.003	0.254	0.215	0.270	-0.159	-0.155	-0.069	-0.041	-0.103	-0.136	-0.116	-0.064	0.251
73.69	-0.229	-0.071	0.227	0.215	0.268	-0.171	-0.154	-0.059	-0.069	-0.114	-0.110	-0.096	-0.077	0.344
74.63	-0.235	-0.080	0.219	0.221	0.272	-0.192	-0.165	-0.048	-0.035	-0.107	-0.100	-0.098	-0.082	0.369

Table A12. Logarithm of the bolometric luminosities integrated over the $uvw2$, $uvvm2$, $uvw1$, U , B , g , V , r , i , z , J , H , K_s , $W1$, $W2$.

rest-frame phase [days]	$\log_{10} L_{\text{bol}}$
-48.01	43.30(0.04)
-38.60	43.61(0.04)
-37.65	43.62(0.04)
-36.16	43.86(0.04)
-35.17	43.87(0.04)
-34.08	43.94(0.04)
-33.90	43.91(0.04)
-31.43	44.07(0.04)
-30.13	44.10(0.04)
-29.65	44.14(0.04)
-29.12	44.14(0.04)
-28.80	44.17(0.04)
-26.71	44.22(0.04)
-26.39	44.22(0.04)
-26.05	44.22(0.04)
-25.91	44.26(0.04)
-25.80	44.24(0.04)
-25.43	44.25(0.04)
-24.50	44.24(0.04)
-22.85	44.29(0.04)
-21.88	44.32(0.04)
-21.87	44.32(0.04)
-21.20	44.31(0.04)
-20.78	44.32(0.04)
-20.08	44.34(0.04)
-15.10	44.35(0.04)
-14.37	44.38(0.04)
-14.17	44.37(0.04)
-13.22	44.38(0.04)
-12.27	44.39(0.04)
-11.68	44.39(0.04)
-10.83	44.40(0.04)
-10.42	44.38(0.04)
-10.30	44.39(0.04)
-9.78	44.40(0.04)
-7.93	44.38(0.04)
-7.56	44.38(0.04)
-7.20	44.38(0.04)
-4.04	44.39(0.04)
-4.02	44.39(0.04)
-3.85	44.39(0.04)
-2.42	44.40(0.04)
-2.28	44.39(0.04)
-1.25	44.38(0.04)
-0.63	44.38(0.04)
0.93	44.38(0.04)
3.18	44.35(0.04)
6.49	44.34(0.04)
11.35	44.29(0.04)
13.21	44.28(0.04)
14.02	44.31(0.04)
15.96	44.30(0.04)
16.08	44.27(0.04)
19.66	44.26(0.04)
21.07	44.24(0.04)
22.30	44.27(0.04)
23.41	44.26(0.04)
24.80	44.24(0.04)
26.25	44.24(0.04)
26.92	44.24(0.04)
29.07	44.21(0.04)
30.44	44.16(0.04)

Table A12. (continued).

rest-frame phase [days]	$\log_{10} L_{\text{bol}}$
30.50	44.21(0.04)
30.94	44.17(0.04)
31.62	44.19(0.04)
34.70	44.17(0.04)
35.66	44.15(0.04)
36.62	44.13(0.04)
37.58	44.15(0.04)
38.22	44.14(0.04)
38.39	44.15(0.04)
38.98	44.15(0.04)
40.35	44.14(0.04)
41.05	44.12(0.04)
41.09	44.10(0.04)
42.22	44.07(0.04)
43.17	44.09(0.04)
45.99	44.05(0.04)
48.82	44.03(0.04)
50.44	44.01(0.04)
52.18	44.02(0.04)
53.27	44.00(0.04)
55.17	43.98(0.04)
61.04	43.92(0.04)
62.79	43.90(0.04)
63.82	43.89(0.04)
66.29	43.86(0.04)
68.53	43.84(0.04)
69.38	43.84(0.04)
72.28	43.81(0.04)
73.75	43.79(0.04)
74.71	43.79(0.04)
75.92	43.77(0.04)
76.06	43.77(0.04)
82.67	43.67(0.04)
87.40	43.65(0.04)
90.23	43.61(0.04)
91.14	43.60(0.04)
94.94	43.58(0.04)
98.69	43.55(0.04)
102.46	43.47(0.04)
240.29	42.62(0.04)
251.57	42.77(0.04)
260.64	42.54(0.04)
270.05	42.57(0.04)
271.39	42.52(0.04)
275.13	42.45(0.04)
348.47	42.15(0.04)
357.89	42.08(0.04)
373.84	42.24(0.04)
374.76	42.22(0.04)
379.45	42.12(0.04)
384.20	42.23(0.04)
385.13	42.18(0.04)
385.13	42.02(0.04)
385.14	42.17(0.04)
414.90	$\geq 42.01(0.04)$

Table A13. Spectra in Fig. 5.

MJD	rest-frame phase [days]	instrumental set-up [grism/grating]	resolution [Å]
58428.57	-34	LCO+FLOYDS	15.5
58429.57	-33	LCO+FLOYDS	15
58430.25	-32	NTT+EFOSC2 [gr13]	18
58433.19	-29	HET+LRS2	-
58436.35	-26	LCO+FLOYDS(*)	15
58437.02	-26	NOT+ALFOSC [gr4]	14
58437.14	-25	NTT+EFOSC2 [gr11+gr16]	15
58440.23	-23	NTT+EFOSC2 [gr11+gr16]	18
58445.41	-18	IRTF+SpeX	-
58446.52	-17	LCO+FLOYDS	-
58450.28	-13	2.4m Hiltner+OSMOS	-
58450.33	-13	HET+LRS2	-
58451.45	-12	LCO+FLOYDS	15
58452.97	-11	NOT+ALFOSC [gr4]	14
58456.79	-8	1.82m+AFOSC [VPH6+VPH7]	15
58458.49	-6	LCO+FLOYDS	15
58460.21	-4	NTT+EFOSC2 [gr11+gr16]	14
58468.16	4	NTT+EFOSC2 [gr11+gr16]	14
58468.47	4	LCO+FLOYDS	15
58474.46	9	LCO+FLOYDS	15
58479.55	14	LCO+FLOYDS	19
58480.81	15	1.82m+AFOSC [VPH6+VPH7]	20
58488.32	23	LCO+FLOYDS	15
58489.87	24	1.82m+AFOSC [VPH6+VPH7]	17
58491.12	25	NTT+EFOSC2 [gr11+gr16]	14
58495.32	29	LCO+FLOYDS	15
58496.89	30	NOT+ALFOSC [gr4]	15
58504.37	38	LCO+FLOYDS	14
58505.86	39	NOT+ALFOSC [gr4]	18
58519.89	52	NOT+ALFOSC [gr4]	14
58522.05	55	NTT+EFOSC2 [gr]	15
58534.87	66	NOT+ALFOSC [gr4]	14
58542.81	73	1.82m+AFOSC [VPH6+VPH7]	14
58543.80	74	1.82m+AFOSC [VPH6+VPH7]	15
58546.28	77	LCO+FLOYDS	15
58559.23	90	LCO+FLOYDS	15
58751.14	269	GTC+OSIRIS [R1000B]	9

(*) This spectrum was not included in Fig. 5 because of its poor signal-to-noise ratio, but it will be made available within the online dataset (see the Data Availability statement).